

RESEARCH ARTICLE

10.1002/2013JB010612

Key Points:

- Earthquakes along the Wilzetta fault have primarily strike-slip focal mechanisms
- The $M5.0$ foreshock encouraged failure along the $M5.7$ mainshock rupture plane

Supporting Information:

- Readme
- Table S1
- Table S2
- Table S3
- Table S4
- Figure S1

Correspondence to:

D. F. Sumy,
dfsuny@gps.caltech.edu

Citation:

Sumy, D. F., E. S. Cochran, K. M. Keranen, M. Wei, and G. A. Abers (2014), Observations of static Coulomb stress triggering of the November 2011 $M5.7$ Oklahoma earthquake sequence, *J. Geophys. Res. Solid Earth*, 119, doi:10.1002/2013JB010612.

Received 19 AUG 2013

Accepted 27 JAN 2014

Accepted article online 6 FEB 2014

Observations of static Coulomb stress triggering of the November 2011 $M5.7$ Oklahoma earthquake sequence

Danielle F. Sumy^{1,2}, Elizabeth S. Cochran³, Katie M. Keranen^{4,5}, Maya Wei⁶, and Geoffrey A. Abers⁷

¹National Science Foundation Earth Sciences Postdoctoral Research Fellow, United States Geological Survey, Pasadena, California, USA, ²Now at Induced Seismicity Consortium, University of Southern California, Los Angeles, California, USA, ³United States Geological Survey, Pasadena, California, USA, ⁴ConocoPhillips School of Geology and Geophysics, University of Oklahoma, Norman, Oklahoma, USA, ⁵Now at Department of Earth and Atmospheric Sciences, Cornell University, Ithaca, New York, USA, ⁶Department of Geological Sciences, Brown University, Providence, Rhode Island, USA, ⁷Lamont-Doherty Earth Observatory, Columbia University, Palisades, New York, USA

Abstract In November 2011, a $M5.0$ earthquake occurred less than a day before a $M5.7$ earthquake near Prague, Oklahoma, which may have promoted failure of the mainshock and thousands of aftershocks along the Wilzetta fault, including a $M5.0$ aftershock. The $M5.0$ foreshock occurred in close proximity to active fluid injection wells; fluid injection can cause a buildup of pore fluid pressure, decrease the fault strength, and may induce earthquakes. *Keranen et al.* [2013] links the $M5.0$ foreshock with fluid injection, but the relationship between the foreshock and successive events has not been investigated. Here we examine the role of coseismic Coulomb stress transfer on earthquakes that follow the $M5.0$ foreshock, including the $M5.7$ mainshock. We resolve the static Coulomb stress change onto the focal mechanism nodal plane that is most consistent with the rupture geometry of the three $M \geq 5.0$ earthquakes, as well as specified receiver fault planes that reflect the regional stress orientation. We find that Coulomb stress is increased, e.g., fault failure is promoted, on the nodal planes of $\sim 60\%$ of the events that have focal mechanism solutions, and more specifically, that the $M5.0$ foreshock promoted failure on the rupture plane of the $M5.7$ mainshock. We test our results over a range of effective coefficient of friction values. Hence, we argue that the $M5.0$ foreshock, induced by fluid injection, potentially triggered a cascading failure of earthquakes along the complex Wilzetta fault system.

1. Introduction

As the population of the United States continues to grow, so does the demand for energy resources. Earthquakes in the continental interior of the United States have historically been rare, yet in 2011 alone, moderate-sized earthquakes occurred in Colorado, Texas, Oklahoma, Ohio, and Arkansas. These earthquakes occurred in close proximity to fluid injection wells, which suggest that ongoing oil and natural gas activities may be to blame [e.g., Horton, 2012; Keranen et al., 2013; Kim, 2013]. The November 2011 Oklahoma sequence includes the largest earthquake ($M5.7$) ever correlated with wastewater injection [Keranen et al., 2013]. These recent events suggest that some fluid injection wells, especially those close to densely populated areas, could pose a significant seismic risk.

In 1993, fluid injection began within oil fields structurally contained by the Wilzetta fault, a complex, ~ 200 km long, Pennsylvanian-aged fault system near Prague, Oklahoma [Way, 1983; Joseph, 1987]. On 5 November 2011, a $M5.0$ earthquake (Event A) ruptured the Wilzetta fault, in close proximity to several injection wells (red and white inverted triangles in Figure 1 [Keranen et al., 2013]). This earthquake was followed less than 24 h later by a $M5.7$ earthquake (Event B; Figure 1), located less than 2 km southwest of Event A. Following Event B, the partial catalog of Keranen et al. [2013] reports over a thousand aftershocks that propagate unilaterally away from the fluid injection wells, including a $M5.0$ aftershock on 8 November 2011 (Event C; Figure 1). All three $M \geq 5.0$ earthquakes exhibit strike-slip fault geometries consistent with rupture on three independent focal planes (Global Centroid Moment Tensor (GCMT) catalog [www.globalcmt.org]), which suggests that three separate portions of the Wilzetta fault system were activated.

The proximity of earthquakes to active fluid injection wells, the unilateral progression of aftershocks away from Event A, and the shallow earthquake depths (83% < 5 km deep; $\sim 20\%$ located within sedimentary units where fluids are injected) led Keranen et al. [2013] to conclude that fluid injection was responsible for

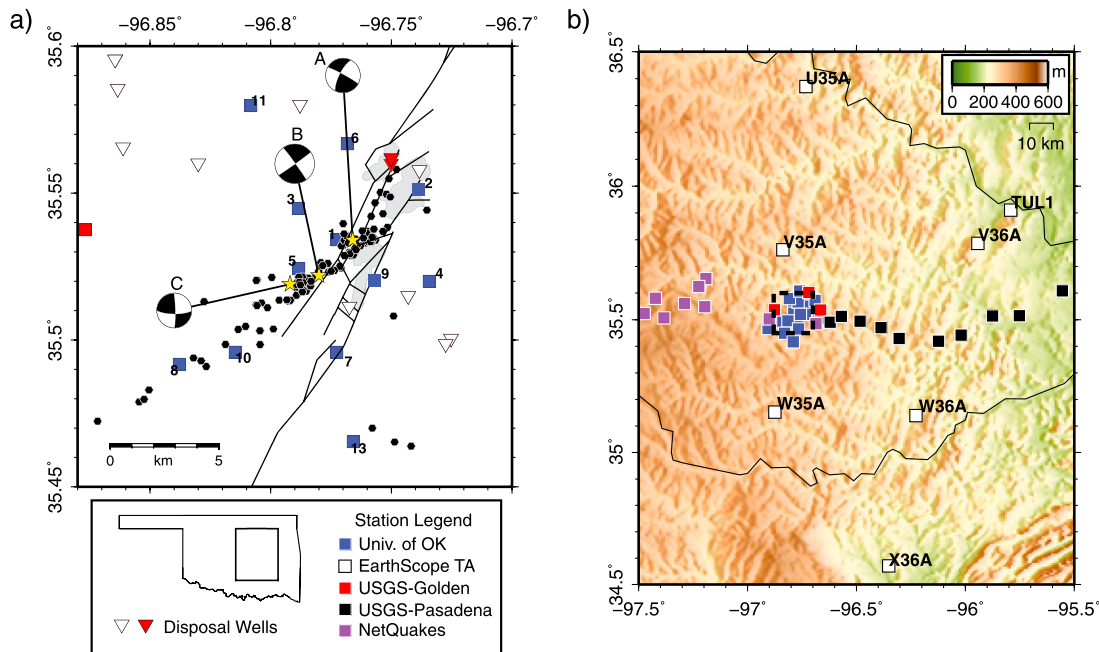


Figure 1. (a) The three $M \geq 5.0$ events (yellow stars), placed at their Oklahoma Geological Survey locations with focal mechanisms from the Global Centroid Moment Tensor catalog. The locations for 110 events with the best quality focal mechanism solutions determined in this study are shown by black dots. The Wilzetta fault system (dark gray lines) is compiled from regional [Joseph, 1987] and detailed local [Way, 1983] studies. Active injection wells close to Event A (red inverted triangles) may be responsible for triggering earthquakes along these faults. Fluid injection takes place within fault-bounded reservoirs (gray shaded regions), depleted from earlier oil and natural gas extraction. Additional nearby fluid injection wells (white inverted triangles) affect the pore pressure and hydrogeologic parameters in this region and complicate the Coulomb fault failure analysis. The University of Oklahoma deployed a total of eighteen stations in the epicentral region; the stations are LC (for Lincoln County, Oklahoma) and their number, but are identified here by number for the sake of clarity. (b) The map shows the 47 stations used in this study, color coded by operating agency as identified in the legend. The EarthScope Transportable Array stations are also labeled. The inset box identifies the region shown in Figure 1a. The inset box within the map of Oklahoma in the legend shows the region identified in this map. Topography data is NASA ASTER data with 10 m resolution in the United States.

triggering the $M5.0$ foreshock. Furthermore, *Llenos and Michael* [2013] used the epidemic-type aftershock sequence model to analyze the catalog of $M > 3$ earthquakes in Oklahoma and observe an increase in the aftershock productivity of earthquakes after 2009; they suggest that an underlying triggering mechanism such as fluid injection may be to blame.

Earthquake activity may be promoted when stress is increased on a fault by as little as 0.1 bar [Stein, 1999]. Small increases in stress due to earlier earthquake activity [e.g., *Harris, 1998; Stein, 1999; King and Cocco, 2001; Steacy et al., 2005*], an increase in pore pressure from fluid injection or reservoir impoundment [e.g., *Nur and Booker, 1972; Zoback and Harjes, 1997; Gahalaut and Hassoup, 2012*], dynamic stress changes due to passing seismic waves [e.g., *Gomberg et al., 2001, 2003*], or even tidal stress [e.g., *Cochran et al., 2004; Stroup et al., 2007, 2009; Crone et al., 2011*] can trigger earthquakes. The last $M5.0$ earthquake in Oklahoma occurred in 1952, and the rare occurrence of three large ($M \geq 5$) earthquakes and numerous aftershocks in Oklahoma suggests that even relatively stable intraplate regions of the brittle continental crust may be critically stressed and near frictional failure [e.g., *Zoback and Harjes, 1997*]. A buildup of pore pressure after ~ 18 years of fluid injection likely triggered the $M5.0$ foreshock [Keranen et al., 2013]; we investigate whether the resulting static stress change from the foreshock may have caused cascading failure [e.g., *Dodge et al., 1995, 1996*] that led to the mainshock and subsequent aftershock sequence.

In this study, we use the Coulomb 3.3 software [Toda et al., 2011b], which implements the elastic half space of *Okada* [1992], to model the static stress changes through time and to investigate whether the $M5.0$ foreshock (Event A) is responsible for the cascading failure of the Wilzetta fault system in Oklahoma. We detect and relocate 110 earthquakes previously identified in the Oklahoma Geological Survey (OGS) catalog and/or the earthquake catalog of *Keranen et al.* [2013] and determine their focal mechanism solutions with the HASH software [Hardebeck and Shearer, 2002, 2003]. We calculate the Coulomb stress change on the nodal planes of these events, as well as determine the regional stress direction from their principal axes. The regional stress direction derived from the focal mechanism solutions provides us with information to determine a specified

fault plane (SFP) that is most favorably oriented for failure; thus, we also calculate the Coulomb stress changes for each aftershock on the SFP orientation. We compare the number of events consistent with Coulomb stress triggering for both the limited set of focal mechanism solutions and for the SFPs of the more complete earthquake catalog. These analyses provide insight into whether the *M*5.0 foreshock (Event A), triggered by injection [Keränen *et al.*, 2013], results in a Coulomb stress change that encourages failure of the *M*5.7 mainshock (Event B) and the subsequent aftershock sequence along the Wilzetta fault system.

2. Coulomb Fault Failure

The brittle failure of faults is thought to be due to the combination of the normal (confining) and shear stress conditions, commonly quantified as the static Coulomb failure criterion [e.g., King *et al.*, 1994]. Static Coulomb stress changes caused by earthquake rupture can help explain the distribution of aftershocks [e.g., Reasenber and Simpson, 1992], as aftershocks will occur when the Coulomb stress exceeds the failure strength of the fault surface. The static Coulomb fault failure (ΔCFF) is defined as

$$\Delta\text{CFF} = \Delta\tau + \mu(\Delta\sigma + \Delta p), \quad (1)$$

where $\Delta\tau$ is the change in shear stress on the fault (positive in the direction of slip), $\Delta\sigma$ is the change in normal stress (positive for fault unclamping), Δp is the change in pore pressure, and μ is the coefficient of friction, which ranges from 0.6 to 0.8 for most intact rocks [see Harris, 1998, and references therein].

In this region of Oklahoma, where fluid injection into 1–2 km deep wells near the foreshock epicenter, has been used to dispose of wastewater since 1993 [e.g., Keränen *et al.*, 2013], the effect of pore pressure cannot be neglected. The pore pressure change immediately after a change in stress, where there is no fluid flow (undrained conditions), is

$$\Delta p = \frac{-\beta\Delta\sigma_{kk}}{3} \quad (2)$$

where β is the Skempton's coefficient and σ_{kk} is the sum of the diagonal elements of the stress tensor [Rice and Cleary, 1976]. The Skempton's coefficient describes the change in pore pressure that results from a change in an externally applied stress and often ranges in value from 0.5 to 1.0 [e.g., Green and Wang, 1986; Hart, 1994; Cocco and Rice, 2002].

For plausible fault zone rheology, where the fault zone materials are more ductile than the surrounding materials, $\sigma_{xx} = \sigma_{yy} = \sigma_{zz}$ [Rice, 1992; Simpson and Reasenber, 1994; Harris, 1998]; thus, $\frac{\Delta\sigma_{kk}}{3} = \Delta\sigma$. Equations (1) and (2) combined with this assumption lead to

$$\Delta\text{CFF} = \Delta\tau + \mu'\Delta\sigma \quad (3)$$

where $\mu' = \mu(1 - \beta)$ is the effective coefficient of friction. The effective coefficient of friction generally ranges from 0.0 to 0.8, but is typically found to be around 0.4 ($\mu = 0.75$, $\beta = 0.47$) for strike-slip faults or faults of unknown orientation [Parsons *et al.*, 1999]; this value is commonly used in calculations of Coulomb stress changes to minimize uncertainty [Stein *et al.*, 1992; King *et al.*, 1994; Toda *et al.*, 2011a].

The location and geometry of the source rupture, as well as the slip distribution over the source plane, play an important role in calculating the Coulomb stress change. Based on earthquake magnitude, we model the source geometry with the empirical relations of Wells and Coppersmith [1994] for strike-slip faults, which are built into the Coulomb 3.3 software [Toda *et al.*, 2011b]. For Events A–C, we use the GCMT reported magnitudes and focal mechanism solutions, and the OGS reported locations for the rupture centroid. We use the OGS locations here instead of the GCMT locations, because the locations are based on proximal station information and have smaller locations errors, more closely match the aftershock distributions, and are more consistent with the regions of highest shaking intensities according to "Did You Feel It?" (<http://earthquake.usgs.gov/earthquakes/dyfi/events/us/b0006klz/us/index.html>). Events A and C (both *M*5.0) have rupture dimensions of ~2.82 km in rupture length and ~2.91 km in rupture width, respectively, while Event B (*M*5.7) has rupture dimensions of ~8.31 km in rupture length and ~5.41 km in rupture width, consistent with the aftershock distribution shown by Keränen *et al.* [2013]. We model Events A and C with ~0.14 m and Event B with ~0.3 m of predominantly strike-slip motion and tapered into five 1 × 1 km nested rectangles of slip to avoid unphysical stress concentrations near the fault ends. The taper used here is the default in the Coulomb 3.3 software; we also test a range of realistic tapers and find that this did not change our results. Finite fault inversion methods [e.g., Liu and Archuleta, 2004, and references therein] could

not be applied to these earthquakes due to their small magnitudes ($M < 7$) and inadequate station coverage before the events; thus, the events are modeled with uniform slip across the rupture surface.

The representations of the “source” faults (faults which have slip), as described above, are used to determine the Coulomb stress change on the “receiver” faults (faults onto which the stress change is resolved). While each earthquake reduces the net regional stress, each event can result in local stress increases that trigger other earthquakes. Aftershock productivity is encouraged when a fault, of specified orientation, experiences a stress increase, especially when the stress change is larger than an assumed threshold value of ~ 0.1 bar (or 0.01 MPa) [Stein, 1999]. This relatively low threshold, compared to background crustal stress levels, suggests that the faults are near failure before the earthquakes [e.g., Stein and Lisowski, 1983; Zoback and Townend, 2001]. Based on this assumed threshold, we examine whether aftershock activity is promoted in regions of stress increase (greater than 0.1 bar stress change), inhibited in regions of stress decrease (less than -0.1 bar stress change), and neither promoted or inhibited in regions where stress changes range between -0.1 and 0.1 bar [e.g., Reasenber and Simpson, 1992]. However, a limitation of the Coulomb stress modeling approach is that it often underestimates the number of aftershocks within the regions of Coulomb stress increase directly adjacent to (within < 5 km of) the fault plane, which is due to assumptions of planar fault geometry and a smooth slip distribution along the fault [e.g., Hardebeck et al., 1998; Smith and Dieterich, 2010].

The parameters in equation (3) need to be considered as a function of time, as the stress distribution from the $M5.0$ foreshock will be different than the stress distribution due to the combination of the $M5.0$ foreshock and $M5.7$ aftershock, and so forth. We therefore consider each $M \geq 5.0$ earthquake (Events A–C) as a “mainshock” that has its own distribution of aftershocks and explore the Coulomb stress distribution and potential triggering of aftershocks through time. Note that due to the short-term (coseismic) time frame taken into consideration, we neglect the alteration of pore pressure caused by the fluid flow in the Coulomb stress modeling, consistent with Beeler et al. [2000] and Cocco and Rice [2002].

3. Earthquake Detection and Location Techniques

In the week that followed Event A (the $M5.0$ foreshock), we deployed 31 continuously recording, three-component seismometers within 100 km of the sequence from the Program for Array Seismic Studies of the Continental Lithosphere (PASSCAL), Rapid Array Mobilization Program (RAMP), the University of Oklahoma (OU), and the United States Geological Survey (USGS) (Figure 1). The temporary instruments augment the existing seven EarthScope Transportable Array (TA) stations [Meltzer et al., 1999] and the nine USGS NetQuakes accelerometers mostly located near Oklahoma City that are configured to trigger on $M > 3.0$ events. Thus, a total of 47 stations recorded the sequence. The partial catalog of Keranen et al. [2013] reports over 800 aftershocks in the days and months following Event A.

In this study, we initially examine 217 earthquakes originally identified in the OGS catalog and/or the catalog of Keranen et al. [2013] that occur between Event A until the end of 2011. We remove the instrument response and apply station specific filters to convert acausal finite impulse response filtered data to causal. Acausal filters can affect the phase onset of the seismic waves and may hinder the proper picking of the phase and polarity information [Scherbaum and Bouin, 1997]. (Appendix A details specifics on the instrument and data logger type, as well as sample rate.) We manually pick visible P wave and S wave arrivals with the Seismic Analysis Code software to improve azimuthal coverage for the focal mechanism analysis compared to the analysis of Keranen et al. [2013]. For each pick, we assess the character of the phase onset (emergent or impulsive) and the quality of the pick (0–4, where 0 is best and 4 is worst). Since polarity information will be important for the focal mechanism analysis, we also assess the first motion for each P wave pick by assigning a positive or negative (up or down) polarity to each pick.

We require P wave and/or S wave picks on a minimum of seven stations for earthquake relocation. With the P wave and S wave pick timing, onset, and quality information, we locate individual earthquakes with the Hypoinverse algorithm [Klein, 2002] based on a one-dimensional P wave velocity model of Keranen et al. [2013] and a P wave-to- S wave velocity ratio of 1.73. On average, we use a combination of 46 P wave and S wave picks to constrain the hypocenters, with the S wave picks weighted at 50% compared to the P wave picks, as the S wave onset is more difficult to determine and can be obscured by the P wave coda. The initial hypocentral location is set to the latitude and longitude of the closest station (i.e., the station with the earliest arrival time) with a trial depth of 5 km. We then perform an initial absolute relocation analysis of the individual earthquakes with the

Velest algorithm [Kissling, 1988; Kissling *et al.*, 1994], which is a technique to improve the hypocentral location and reduce the root-mean-square (RMS) travel time residuals. We further refine the event locations in a relative sense with the *hypoDD* double-difference algorithm [Waldhauser and Ellsworth, 2000; Waldhauser, 2001]. The *hypoDD* algorithm iteratively solves for hypocentral variations, in a least squares sense, by minimizing the residuals of travel times between pairs of nearby events recorded on a common station, thus removing bias due to velocity model errors. (For a detailed description of these procedures, the reader is referred to the works of Sumy *et al.* [2013] and Kroll *et al.* [2013]). The hypocenters of the 110 events for which high-quality focal mechanism solutions are determined (discussed in the next section), including their relative relocation errors and travel time residuals, are listed in Appendix B. In general, the relative relocation errors and travel time residuals significantly decrease for events later in the sequence that occur after the installation of additional stations (i.e., recorded by more stations). For the 72 events also cataloged by Keranen *et al.* [2013], the epicentral locations differ by ~ 400 m on average, while the remaining 38 events only cataloged by the OGS differ by ~ 1.3 km on average.

4. Focal Mechanism Determination

We determine focal mechanism solutions from the *P* wave polarity (first-motion) picks and *S/P* amplitude ratios with the program HASH [Hardebeck and Shearer, 2002, 2003]. The HASH algorithm computes takeoff angles from source to receiver and performs a grid search over all possible focal mechanisms to identify the acceptable set of solutions for each earthquake. One benefit of using HASH over other focal mechanism algorithms, such as FPFIT [Reasenber and Oppenheimer, 1985], is that it takes into account possible uncertainties in the polarity information and takeoff angles, which could be affected by errors in the hypocenter location and velocity model. The preferred focal mechanism solution and its uncertainties are defined as the average and spread of the set of acceptable focal mechanisms, respectively.

We use the manually picked *P* wave polarities from the earthquake detection and relocation analysis, as described above. The default in HASH is polarity information from at least eight stations (for at least two station measurements in each quadrant); however, we require a minimum of seven polarities to determine a focal mechanism solution. This allows us the potential to solve for focal mechanisms when only the EarthScope TA stations are available, as they provide favorable azimuthal station coverage especially during the early part of the sequence when very few temporary stations are deployed. We did not restrict mechanisms based on azimuthal station gap or takeoff angle at this stage. In addition, we modify the HASH algorithm to minimize the number of misfit high-quality polarity picks (0–1 quality; 100% and 75% weighting, respectively); HASH traditionally uses impulsive arrivals only, regardless of pick quality. We estimate pick error to be around 5%, which is the percentage of outlier picks thrown out by the *hypoDD* double-difference analysis.

To further refine these mechanisms, we calculate the *S/P* amplitude ratio. The *S/P* amplitude ratio is generally independent of path effects, site effects, or instrument response and is to first order, directly proportional to the seismic energy radiation pattern about the focal sphere [Hardebeck and Shearer, 2003]. The *S/P* amplitude ratio reaches a peak value near the nodal planes, where the *P* wave amplitude becomes small while the *S* wave amplitude is large. Furthermore, the *S/P* amplitude ratio becomes small near the *P* (most compressive) and *T* (least compressive) axes, where the *P* wave polarities are large and *S* wave radiation reaches a minimum. The *S/P* amplitude ratio used in conjunction with the *P* wave polarity information can thus provide better constraints on the focal mechanism solutions, since the amplitudes have a range of values and can more precisely constrain the location of the observation on the focal sphere [e.g., Hardebeck and Shearer, 2003].

To calculate *P* wave and *S* wave amplitudes, we filter the three-component waveforms above 1 Hz frequency to remove low-amplitude, long-period noise. We use the *P* wave and *S* wave arrival times to select windows for the *S/P* amplitude ratio measurement, because it is one of the most robust and simplest approaches [Hardebeck and Shearer, 2003; Yang *et al.*, 2012]. For the *P* wave, the noise window is between -2.5 and -0.5 s before the *P* wave and the signal window starts 10% of the *S-P* time (in s) before the *P* pick and ends 50% of the *S-P* time (in s) after the *P* wave pick (Figure 2). For the *S* wave, the noise window is from 50% to 75% of the *S-P* time before the *S* wave pick and the signal window is from 10% of the *S-P* time before to 100% of the *S-P* time after the *S* wave pick (Figure 2). We choose to use a percentage of the *S-P* time for the window lengths, because the time between the *P* and *S* arrivals varies significantly across the network (~ 4 s on average); we wanted to ensure that we had appropriately short windows for nearby stations (with < 1 s *S-P* times) while still recording the peak amplitudes at more distant stations that have longer-period energy. We use the peak-to-peak difference in each

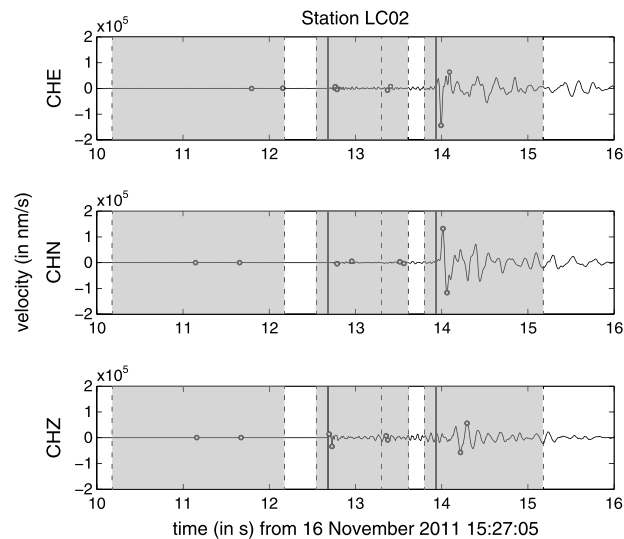


Figure 2. Three-component velocity waveforms (in nm/s) for a $M_{2.7}$ event on 16 November 2011, recorded by station LC02 (annotated in Figure 1a). Gray windows show periods where peak-to-peak noise is measured before the P wave and S wave arrivals and for the P wave and S wave signals, respectively. Dashed lines mark the temporal extent of each window; note that the noise window before the S wave arrival begins where the P wave arrival window ends (discussed in the text). For each window, the dots mark the maximum and minimum amplitudes. The two solid lines show the picks of the P wave (~ 11.65 s) and the S wave (~ 12.9 s), respectively.

plane uncertainties is the best single indicator for focal mechanism quality [Kilb and Hardebeck, 2006]. The quality of the focal mechanisms also depends on how well our observations cover the focal sphere or the azimuthal gap between stations. If the azimuthal gap is large, our knowledge of the focal sphere, and thus the correct focal mechanism, will be limited, regardless of the number of observations. Thus, we base the quality of our mechanisms (A: best; D: worst) on the mean nodal plane uncertainty and the azimuthal station gap, like Yang *et al.* [2012]. We focus on the 110 events with A and B quality focal mechanism solutions, which have mean nodal plane uncertainties of $\leq 25^\circ$ and 25° – 35° , respectively, and have azimuthal station gaps of $\leq 90^\circ$. The 95 A quality and 15 B quality focal mechanism solutions are shown in Figure 4 and listed in Appendix C.

Within a strike variation of $\leq 25^\circ$ (the maximum mean nodal plane uncertainty of A quality mechanisms), 69 events ($\sim 63\%$ of the focal mechanisms) have at least one nodal plane consistent with the GCMT-determined rupture planes of Events A and B (black colored focal mechanisms in Figure 4), and 24 events ($\sim 22\%$ of the focal mechanisms) have at least one nodal plane consistent with the GCMT-determined rupture along the fault plane of Event C (gray colored focal mechanisms in Figure 4). The remaining 17 earthquakes (14% of the mechanisms; $M_{0.7}$ – 3.5) are considered anomalous, as these earthquakes have either dip-slip mechanisms (dip $\leq 65^\circ$) and/or a rupture plane inconsistent with the orientation of Events A–C (magenta colored focal mechanisms in Figure 4). In regions of complicated fault geometry like the Wilzetta fault system, dip-slip mechanisms tend to occur within regions where the faults link together and could be due to the change in stress orientation from one fault to the other [Engeln *et al.*, 1986; Sumy *et al.*, 2013].

5. Coulomb Stress Changes Derived on Assumed Rupture Planes

We calculate Coulomb stress changes on the nodal planes of the 110 high-quality focal mechanism solutions in their rake directions (Figure 5). The calculation of Coulomb stress changes on the nodal planes of aftershock focal mechanism solutions is a strict test of the Coulomb hypothesis, as it requires no assumptions about the regional stress state or aftershock fault geometry [Toda *et al.*, 2011a]. Shear stress changes are similar on either nodal plane, but normal stress changes will vary [Hardebeck *et al.*, 1998]; thus, we calculate the Coulomb stress change on the nodal plane that is most consistent with the orientation of rupture for the three largest events (Events A–C).

window and apply a vector summation across all three components to obtain the noise and signal amplitudes, respectively [Yang *et al.*, 2012]. For HASH, the minimum S/P amplitude ratio for use in the focal mechanism calculation is set at 3.0, and the acceptable variation in the S/P amplitude ratio as a result of noise is set at 0.3 in \log_{10} scale, which is consistent with other studies [i.e., Hardebeck and Shearer, 2003; Yang *et al.*, 2012].

We use a 5° angle step across strike, dip, and rake to search for all possible solutions and show an example of the set of all possible solutions (gray nodal planes) and the preferred solution (black nodal planes) for the P wave polarities alone and the combination of P wave polarities and S/P amplitude information, respectively, in Figure 3. The root-mean-square angular difference between the acceptable nodal planes and the preferred nodal plane is the nodal plane uncertainty [Hardebeck and Shearer, 2002; Yang *et al.*, 2012]. The mean of the nodal

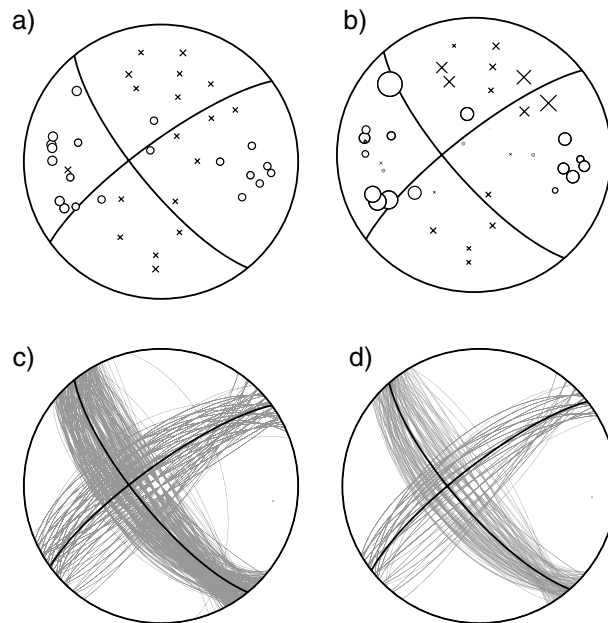


Figure 3. The focal mechanism solutions for a $M_{2.7}$ event on 16 November 2011 (same as Figure 2) with (a) P wave polarity information only and (b) with both P wave polarity and S/P amplitude ratio information, respectively. Stations are projected onto a stereonet, where compressional (up) polarities are indicated with an “x” and the dilatational (down) polarities with an open circle. For stations with S/P amplitude ratio information, the symbols are scaled by their $\log_{10} S/P$ amplitude. Stations with polarity information only are shown by small gray symbols in Figure 3b. The distribution of acceptable focal mechanism solutions (gray curves) and the preferred solution (black curve) for (c) P -polarity information only, and (d) for both P polarity and S/P amplitude ratios. We report the preferred solution for this event (event #86) in Table C1.

We find that Event A exerts an ~ 1.3 bar Coulomb stress increase on the hypocenter of Event B, resolved onto the fault plane. This finding suggests that while fluid injection may have triggered the $M_{5.0}$ foreshock (Event A) [Keranan *et al.*, 2013], Event A likely triggered the $M_{5.7}$ mainshock (Event B). Events A and B however exert an ~ 5.6 bar negative Coulomb stress change on the GCMT focal mechanism solution for Event C. In Table 1, we report the number of earthquakes that are promoted (Coulomb fault failure (ΔCFF) > 0.1 bar; red epicenters in Figure 5), inhibited ($\Delta CFF < -0.1$ bar; blue epicenters in Figure 5), or neither ($-0.1 \text{ bar} \leq \Delta CFF \leq 0.1 \text{ bar}$; white epicenters in Figure 5) as a function of time and focal mechanism (i.e., consistent with Events A–C or anomalous). Overall, we observe that $\sim 60\%$ of the earthquakes experience positive Coulomb stress change that would promote failure and $\sim 40\%$ of the aftershocks show negative Coulomb stress change that would inhibit failure for Coulomb stress change resolved onto the earthquake nodal plane. We also find that the percentage is robust, as it does not change even when we examine the maximum Coulomb stress change on either nodal plane.

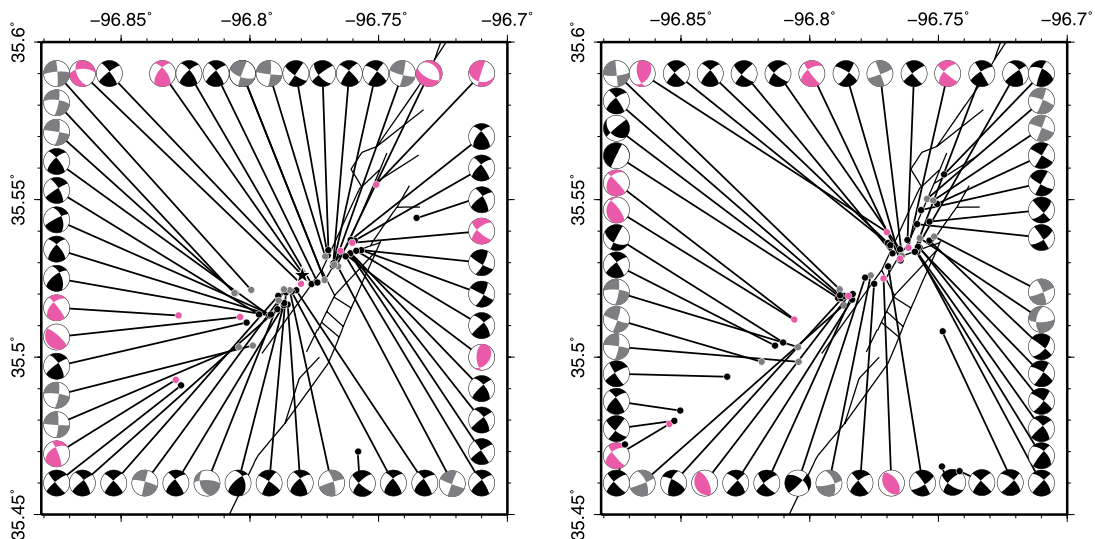


Figure 4. Focal mechanism solutions for the 110 earthquakes with A or B quality mechanisms computed with the HASH software, including the focal mechanism solution for the $M_{5.7}$ mainshock (epicenter shown by a black star). These solutions use both first-motion polarities and S/P amplitude ratios. Focal mechanisms with at least one nodal plane consistent with the rupture planes of Events A or B are shown in black, and those consistent with the rupture plane of Event C are shown in gray. Anomalous earthquakes (as defined in the text) are shown with magenta focal mechanism solutions. The earthquakes are split between two maps for the sake of clarity.

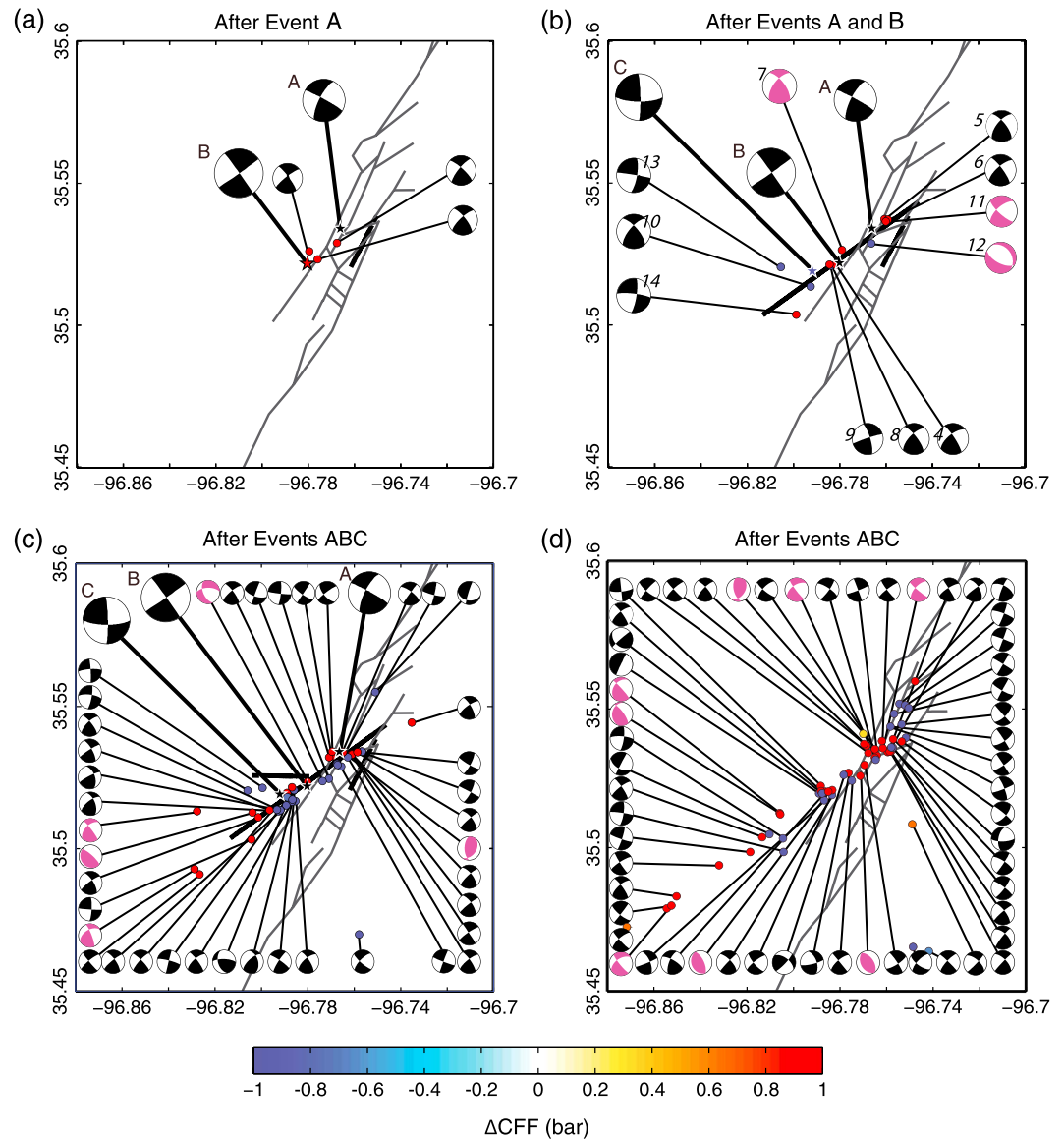


Figure 5. The Coulomb fault failure shown for the focal mechanism solutions for (a) earthquakes after Event A, including our focal mechanism solution of the $M_{5.7}$ mainshock (Event B), which is denoted by "HB" (or HASH Event B); (b) earthquakes after Events A and B, labeled with their event number (Tables B1 and C1), and (c and d) earthquakes after Events A–C. The earthquake epicenters are color coded by its ΔCFF , in bar.

To further test our results, we examine a range of effective coefficient of friction values (μ') between 0.0 and 0.8 (Table S1 in the supporting information), which includes the shear stress change alone ($\mu' = 0.0$). The shear stress change ($\Delta\tau$) does not depend on which rupture plane is considered, nor does it depend on the coefficient of friction we choose. In addition, we perform 2000 random resamples of the focal mechanism solutions for each earthquake (Table S2 in the supporting information), where the event location is kept constant and the focal mechanism solutions are randomly subsampled from the existing set. We observe the same distribution of earthquakes, in that 60% of earthquakes lie within the regions of Coulomb stress increase and 40% lie within the regions of Coulomb stress decrease, regardless of the effective coefficient of friction and/or the particular focal mechanism from the set. Thus, we find that the percentage of events that are encouraged is robust, regardless of slight changes in fault orientation away from the rupture planes of the three $M \geq 5.0$ events; in fact, *Parsons* [2002] observed this same percentage in a global study of $M_s \geq 7.0$ earthquakes that occurred outside of the classical aftershock zone, which may suggest this ratio persists across many spatial scales of earthquake catalogs.

Table 1. Δ CFF (in bars) Computed on Inferred Rupture Plane for A and B Quality Focal Mechanisms

Event	Number of Aftershocks	Δ CFF < -0.1	$-0.1 \leq \Delta$ CFF ≤ 0.1	Δ CFF > 0.1
Event A	3	0 (0%)	0 (0%)	3 (100%)
Event B (Normal)	8	3 (37.5%)	0 (0%)	5 (62.5%)
Event B (Anomalous)	3	1 (33.3%)	0 (0%)	2 (66.6%)
Event B (Total)	11	4 (36%)	0 (0%)	7 (64%)
Event C (Normal)	82	40 (49%)	0 (0%)	42 (51%)
Event C (Anomalous)	14	1 (7%)	0 (0%)	13 (93%)
Event C (Total)	96	41 (43%)	0 (0%)	55 (57%)
TOTAL	110	45 (41%)	0 (0%)	65 (59%)

One might expect that a greater number of the events would have a positive Coulomb stress change resolved onto their nodal planes. The observed distribution most likely reflects a limitation of the Coulomb stress model, in that stresses near the causative fault plane are predicted to decrease when resolved on the prescribed fault geometry consistent with the mainshock [Hainzl *et al.*, 2009]; thus, we observe that ~40% of the focal mechanism solutions are modeled with negative Coulomb stress changes. In effect, our Coulomb model predicts no aftershocks along the main fault plane due to the assumption of uniform stress drop across the rupture surface and a perfectly planar fault; please refer to the discussion section below. It is important to note that while many of the focal mechanism solutions exhibit similar geometry to the $M \geq 5$ earthquake rupture planes, small changes in the receiver fault geometry could significantly affect the Coulomb stress calculation. Thus, we investigate the Coulomb stress change for the earthquake catalog reported by Keranen *et al.* [2013], with the assumption that each earthquake has a focal mechanism consistent with the regional stress orientation.

6. Coulomb Stress Changes Estimated on Specified Receiver Fault Planes

In this section, we examine the Coulomb stress change on specified receiver fault planes (SFPs), which for our study are those expected to fail based on the regional stress direction. This analysis differs from “optimally oriented” fault planes (OOPs), as it removes any dependence on the regional stress amplitude, which can result in a local, often small, rotation in the fault plane orientation in the near-field region of a large-magnitude earthquake [e.g., King *et al.*, 1994; Harris, 1998]. Many of our focal mechanism solutions (~85% of the catalog; Table 1) are consistent with the rupture of the $M \geq 5$ events, which contradicts the assumption of local rotation of the fault plane near the source rupture. We therefore examine the Coulomb stress change on earthquakes from the catalog of Keranen *et al.* [2013] following Events A and B on the SFP consistent with the regional stress direction, without regard for the regional stress amplitude.

To define the regional stress direction, we use the 110 focal mechanism solutions from the aftershock sequence (Figure 4 and Appendix C) to find the azimuth and plunge of the principal stress directions with the methods described by Michael [1984] and Hardebeck and Michael [2006]. As a first pass, we plot the P and T axes (or the most and least compressive stress directions, respectively) of each focal mechanism solution in Figure 6a. The use of P and T axes from the focal mechanisms however more closely represents the moment tensor and not the stress tensor. Thus, we perform a regional-scale stress inversion for the 110 focal mechanism solutions, with the nodal plane that is most consistent with the rupture orientation and aftershock distribution of Events A–C [e.g., Michael, 1987]. We find that on average, the azimuth and plunge for σ_1 (most compressive stress direction) is $\sim 80^\circ$ and $\sim 5^\circ$, for σ_2 (intermediate stress direction) is approximately -21° and $\sim 65^\circ$, and lastly, for σ_3 (least compressive stress direction) is $\sim 172^\circ$ and $\sim 24^\circ$, respectively (Figure 6b). The best stress inversion results along with the 95% confidence interval after 2000 bootstrap resamples are shown in Figure 6b. We assume for the stress uncertainty analysis that 90% of the nodal planes of the focal mechanism solutions are correctly identified as the rupture plane [i.e., Hardebeck and Shearer, 2002, 2003]. Based on the regional stress orientation, the SFP has a nodal plane with a strike of 214° , which is most consistent with the inferred rupture orientation of Events A and B (Figure 6c).

To further test whether Event A triggered subsequent seismicity, we calculate the Coulomb stress change as a function of time on a $0.5 \text{ km} \times 0.5 \text{ km}$ horizontal grid at 1 km depth intervals between 0 and 10 km, which covers the entire depth range of the aftershocks we relocate here, as well as those in the catalog of Keranen *et al.* [2013]. We associate each aftershock in the catalog of Keranen *et al.* [2013] to the closest grid node to estimate the Coulomb stress change at the event’s hypocentral location (Figures 7a and 7b). We find that ~55% of the

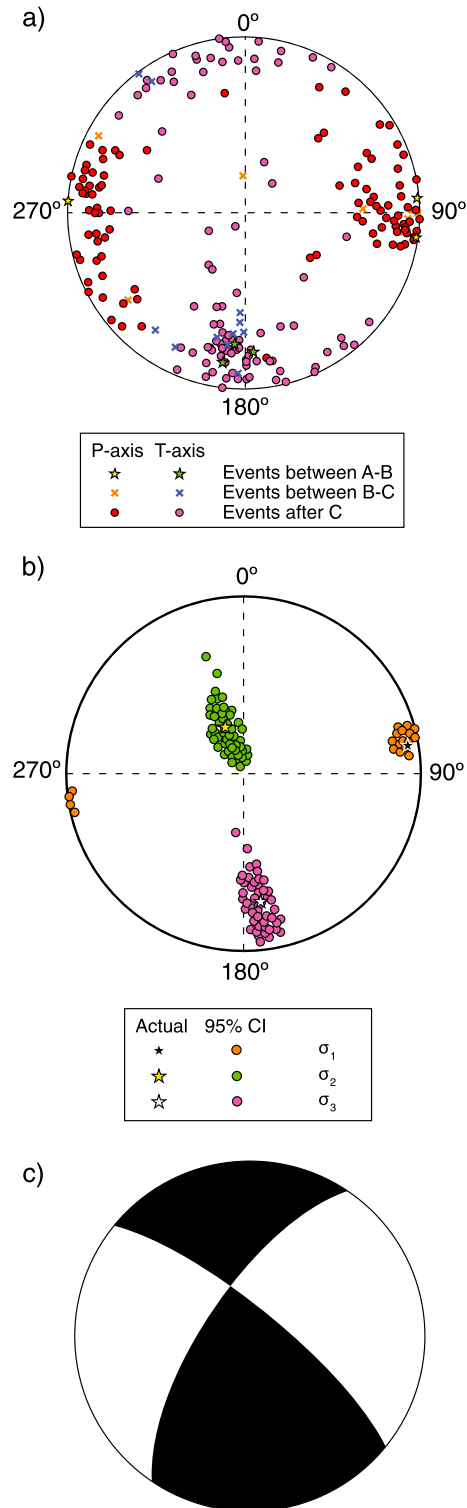


Figure 6. (a) Stereographic projection of the P axis and T axis orientations of the 110 focal mechanisms, color coded by time as defined in the legend. (b) The stress inversion solution for the most compressive (σ_1 , black star), intermediate (σ_2 , yellow star), and least compressive (σ_3 , white star) principal stress axes. The 95% confidence intervals after 2000 bootstrap resamples are color coded by axis and defined in the legend. The relative stress ratio (φ) is 0.24, with a 95% confidence interval between 0.07 and 0.48. (c) The best fit regional focal mechanism solution based on the stress inversion. The focal mechanism is most consistent with the focal mechanism solutions of Events A and B.

earthquakes that occurred between the $M5.0$ foreshock (Event A) and the $M5.7$ mainshock (Event B) occurred within the regions where the estimated Coulomb stress change resolved onto the SFPs is positive and would promote failure (Figure 7a and Table 2). Thus, we observe that Event A triggered the majority of earthquakes up through Event B. However, for the 182 earthquakes that occurred between the $M5.7$ mainshock (Event B) and the $M5.0$ aftershock (Event C), only 23% lie within the regions of Coulomb stress increase (Figure 7b).

To further test our results, we examine the Coulomb stress change on the SFP as a function of the effective coefficient of friction (μ') and find that ~55–63% and ~23–31% of the earthquakes fall within the regions of Coulomb stress increase following Event A and Event B, respectively (Table S3 in the supporting information). Thus, for SFP, the effective coefficient of friction only results in a slight (<10%) change in the number of events that fall into regions of Coulomb stress increase or decrease. Furthermore, we calculate the Coulomb stress change on earthquakes between Events A and B as if they had the same rupture plane orientation of the GCMT solution of Event B and on earthquakes between Events B and C as if they had the same rupture plane orientation of the GCMT solution of Event C, respectively (Figures 7c–7d). We find similar results to the SFP analysis described above; in that, ~76% of aftershocks occur within the regions of Coulomb stress increase following Event A and that only ~35% of aftershocks occur within regions of Coulomb stress increase following Event B (Table 2).

Again, we test our results as a function of the effective coefficient of friction (μ') and find that ~58–66% of the earthquakes that occur between Events B and C locate within the regions of Coulomb stress increase when μ' is 0.0–0.2. When the effective coefficient of friction is larger (0.4–1.0), the percentage is dramatically reduced to ~20–35% (Table S3 in the supporting information). Thus, when we use the GCMT rupture plane orientations, we find that the results are more sensitive to the effective coefficient of friction value chosen, with ~40% more events experiencing Coulomb stress increase when μ' is 0 compared to when μ' is 1.0. In this region, we might expect a low effective coefficient of friction if fluid from injection is migrating along the fault, which would cause an increase in pore pressure. An increase in pore pressure would reduce the normal stress along the fault and drive the fault toward failure. In addition, an effective coefficient of friction of zero represents the contribution of the shear stress alone, which would be the same along either nodal plane, and thus removes any nodal plane ambiguity. The shear stress change may provide the most stringent test of the Coulomb stress change following the $M5.7$ mainshock (Event B), as many of the focal mechanism solutions of earthquakes between Events A and B (Figure 5b) are either consistent with Event B or C or exhibit a slight rotation (within 25°) away from these rupture planes. Thus, at low effective coefficients of friction, we find that earthquakes that occur between Events B and C are consistent with triggering by the static Coulomb stress change that results from the contribution of the foreshock and mainshock (Events A and B combined) when considered on the GCMT focal mechanism orientation of Event C; however, this result is not confirmed by the SFP geometry for earthquakes following Event B (Table S3 in the supporting information).

As a final test of our Coulomb stress change modeling, we assign each of the aftershock hypocenters (Figure S1 in the supporting information), with the 110 focal mechanism solutions estimated in this study. For example, there are a total of 21,890 unique focal mechanism-hypocenter combinations for 199 earthquakes that occur between Events A and B, respectively. We find that 62% of the earthquakes that occur between Events A and B locate within regions of Coulomb stress increase, while only ~31% and 37% fall within regions of Coulomb stress increase following Events B and C, respectively (Figure S1 and Table S4 in the supporting information). Overall, the result of these tests suggests that the $M5.0$ foreshock (Event A) triggered the majority of its own aftershocks up through the $M5.7$ mainshock (Event B); however, again, the modeling suggests that the combination of Events A and B may not have triggered subsequent events, which we will discuss in greater detail below.

7. Discussion

In this study, we find that the Coulomb stress change at the location of the $M5.7$ mainshock (Event B) is consistent with triggering by the $M5.0$ foreshock (Event A). This result is upheld through various tests of the method, including Coulomb stress change analysis on the focal mechanism solutions of 110 earthquakes, on the specified fault plane orientation derived from the regional stress inversion of these focal mechanism solutions, as well as on the GCMT focal mechanism solutions of the major $M \geq 5.0$ earthquakes. However, we also find that Events A and B impart a negative Coulomb stress change on the $M5.0$ aftershock (Event C). Even

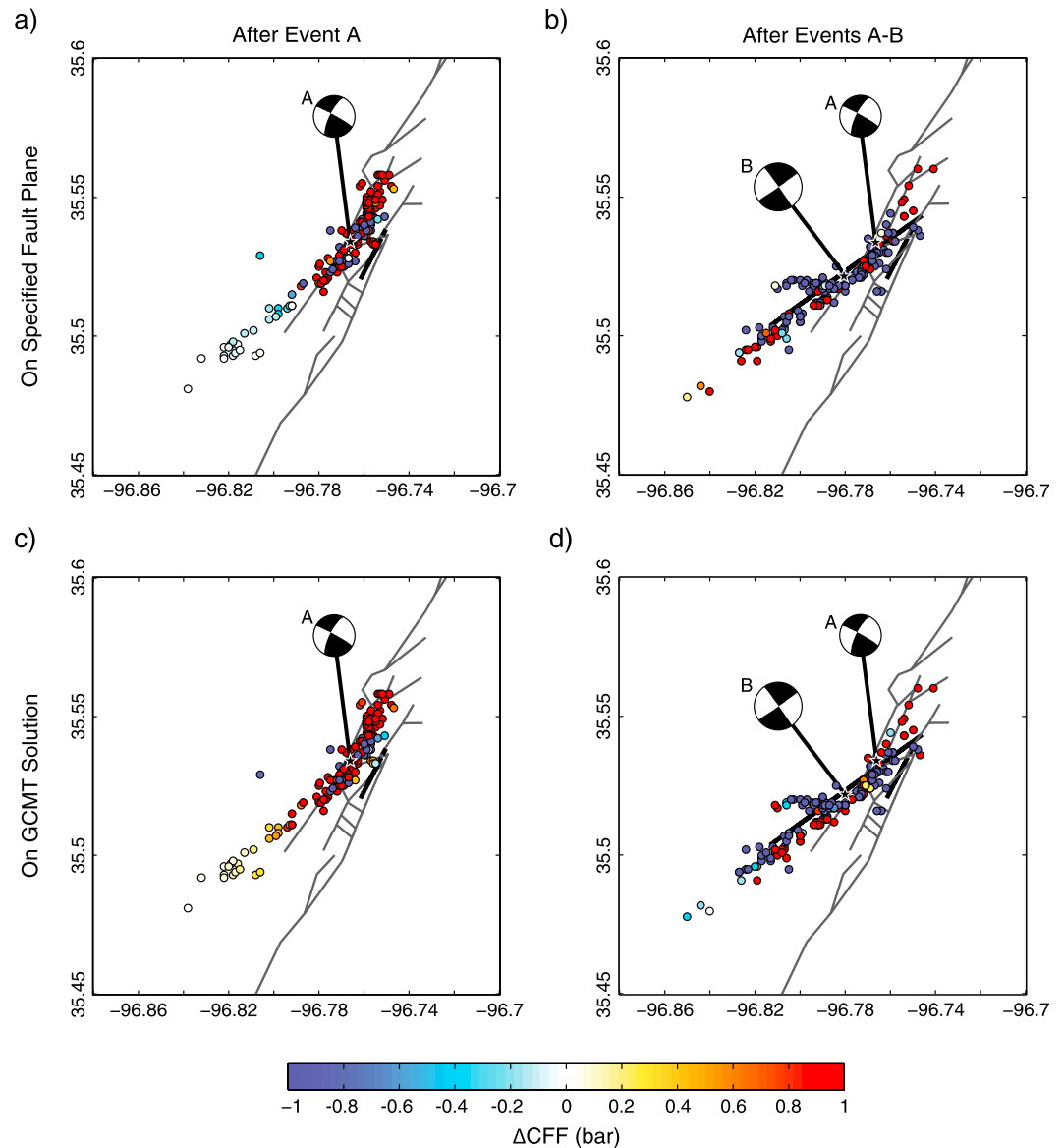


Figure 7. The Coulomb stress change (ΔCFF) is mapped on specified fault planes on the aftershocks that follow (a) the $M5.0$ foreshock (Event A) and (b) the $M5.7$ mainshock (Event B). In addition, we also examine the ΔCFF on the GCMT solutions for (c) the aftershocks of Event A on the GCMT solution of Event B and (d) the aftershocks of Event B on the GCMT solution of the $M5.0$ aftershock (Event C), respectively. Thick black lines represent the surface projection of the rupture planes of each $M \geq 5.0$ earthquake. The aftershocks are color coded by the Coulomb stress change calculated on its closest grid point ($\sim 0.5 \times 0.5 \times 10$ km) in space, as a function of depth and averaged over the entire seismogenic depth from 0 to 10 km.

when the Coulomb stress change that results from Event A alone is considered on the rupture plane of Event C, the net effect is an ~ 2.9 bar Coulomb stress decrease.

These findings beg the question as to why the rupture fault plane of Event C is activated in the first place, since its rupture orientation is so different from that of Events A and B. Many of the focal mechanism solutions in the sequence are consistent with the right-lateral strike-slip orientation of Events A and B; however, several events are also consistent with that of Event C (Figure 4). Furthermore, some of the events have nodal planes that are rotated away from either Events A and B or from Event C resulting in an ambiguity in which nodal plane is the correct rupture plane orientation. This observation, as well as the presence of some dip-slip focal mechanisms, suggests that there are complex rupture geometries present due to the interconnected fault system [e.g., Way, 1983; Joseph, 1987]. Interestingly, aftershocks that follow Event B (Figures 7b and 7d and Figure S1 in the supporting information) also appear along the fault plane that fails in Event C; this observation suggests that this fault plane is

Table 2. Coulomb Stress Change for Aftershocks ($\mu' = 0.4$)

Events	Number of Aftershocks	$\Delta\text{CFF} < -0.1$	$-0.1 \leq \Delta\text{CFF} \leq 0.1$	$\Delta\text{CFF} > 0.1$
<i>On Specified Receiver Fault Planes</i>				
Following Event A	199	67 (34%)	23 (12%)	109 (55%)
Following Event B	182	133 (73%)	7 (4%)	42 (23%)
<i>On Global Centroid Moment Tensor Solutions</i>				
Following Event A on Event B	199	41 (21%)	6 (3%)	152 (76%)
Following Events A–B on Event C	182	117 (64%)	1 (1%)	64 (35%)

activated prior to Event C, although the fault plane is not oriented for failure based on the regional stress direction (Figure 6c). Many of the earthquakes along the rupture plane of Event C show an apparent Coulomb stress decrease (Figures 7b and 7d). The modeling results suggest that the static Coulomb stress change from Events A and B do not trigger Event C. This may suggest that other processes like dynamic stress triggering [e.g., *Felzer and Brodsky, 2005*] and/or an increase in pore pressure due to fluid flow [e.g., *Cocco and Rice, 2002*] are to blame for this event. However, this result more likely reflects the limitations of near-field Coulomb stress modeling with respect to the proximity of earthquakes to one another as well as to the ruptured fault surface.

In general, a large-magnitude earthquake decreases the stress along a fault, yet we observe the greatest number of aftershocks close to the ruptured surface. This observation seems to defy the concept of static stress triggering; however, small-scale heterogeneities along the ruptured surface result in patches of stress increase along the fault, which play a role in the promotion of aftershock activity [e.g., *Hainzl et al., 2010*]. Stress changes caused by a major earthquake are difficult to estimate close to the fault, as there exists small-scale slip variability along the rupture interface [e.g., *Helmstetter and Shaw, 2006; Marsan, 2006*], nonplanar fault geometry [*Smith and Dieterich, 2010*] and heterogeneous pre-rupture stresses. Since differential stress ultimately drives earthquake activity, spatial clustering of aftershocks may in fact result from the distribution of high- and low-stress regions [e.g., *Parsons, 2008; Parsons et al., 2012*]; thus, we might expect aftershocks to also occur within regions of apparent Coulomb stress decrease [e.g., *Stacy et al., 2004; Hainzl and Marsan, 2008*]. Even with the most sophisticated slip models, the lack of information about the stress and slip distribution along the fault plane led *Hardebeck et al. [1998]* to conclude that Coulomb fault failure would be unable to predict the occurrence of near-fault aftershocks (<5 km away from the causative fault).

Here we assume uniform stress drop across the entire rupture surface, as a lack of local stations (for Event A) or lack of nearby on-scale recording (for Events B and C), and relatively small magnitudes of the earthquakes preclude detailed knowledge of the slip along the fault planes of Events A–C. A finite fault inversion of slip for Events B and C is the subject of ongoing research [Shengji Wei, personal communication, 2013] and is out of the scope of this manuscript. In addition, we model the ruptures as simple planar faults, as the small-scale geometry of the fault planes is unknown; *Smith and Dieterich [2010]* show that very small-scale deviations from a perfectly planar fault result in large stress heterogeneities near the fault. Most of the earthquakes locate very close to the fault planes of Events A, B, and C (within <5 km), so a significant portion of the events are modeled to have negative Coulomb stress changes. This includes the *M*5.0 aftershock (Event C), whose rupture plane abuts up against that of Event B (Figure S1c in the supporting information).

In addition, we only model the effect of the largest three events in the earthquake sequence and do not investigate the multiple complex stress interactions between the aftershocks themselves. The next largest magnitude earthquake in our catalog, besides the three $M \geq 5.0$ earthquakes, is a *M*4.0 earthquake (event #4 in Tables B1 and C1). Stress maps are considered stable as long as the largest aftershocks are considered down to a level of $M_{max}-1.5$ [*Hainzl et al., 2010*]. Thus, for our stress maps to be stable, we consider only the three earthquakes of *M*4.2 and larger (*M*5.0 foreshock, *M*5.7 mainshock, and *M*5.0 aftershock). In addition, small errors in the aftershock location could also contribute to our observation that some earthquakes occur when Coulomb stress changes suggest failure would be inhibited (Figures 5 and 7).

When a realistic slip distribution and background stress field is considered, a highly variable suite of failure planes is expected, such that a variety of aftershock mechanisms occur within a kilometer or less of one another [e.g., *Kilb et al., 1997*]. Although many of the focal mechanism solutions in our study are consistent with the rupture planes of Events A–C, anomalous focal mechanism solutions (Figure 5) may provide additional evidence of complex fault interactions and fault geometry. The variability in the focal mechanism solutions of aftershocks, and therefore incomplete knowledge of the receiver fault geometry, may present an additional limitation of our study.

In Oklahoma, the poroelastic response from fluid injection is also important to consider as an external trigger of earthquakes in this region. The instantaneous coseismic stress changes that we model here represent a “snapshot” of the Coulomb stress field immediately following each $M \geq 5$ earthquake, and coseismic stress changes occur on a time scale that is too short to allow for the loss or gain of pore fluid by diffusive transport (fluid flow) [Rice and Cleary, 1976; Cocco and Rice, 2002]. Poroelastic strain transfer has shown to initiate earthquakes along OOPs [Nur and Booker, 1972; Zoback and Harjes, 1997; Shapiro et al., 2006; Guglielmi et al., 2008; Durand et al., 2010; Daniel et al., 2011]; however, these small transient strains (< 1 MPa) may die off too quickly and therefore be insufficient to trigger subsequent earthquake activity [Hainzl and Ogata, 2005].

8. Summary and Conclusions

In summary, we detect and locate 110 earthquakes that have sufficient P wave polarity and S/P amplitude ratio information that is suitable for high-quality focal mechanism solutions. The focal mechanism solutions are predominantly consistent with the inferred strike-slip rupture plane orientation of Events A–C (~85% of the catalog; Table C1); however, the remaining 15% of the events that exhibit variations in strike and anomalous dip-slip focal mechanism solutions may reflect the complex fault geometry in the epicentral region. We calculate the Coulomb stress changes on the inferred rupture plane of the focal mechanism solutions and find that ~60% of the aftershocks including the $M5.7$ mainshock (Event B) occur within the regions of stress increase (> 0.1 bar). Since most of the aftershocks occur close to the ruptured portions of the fault plane (on average, < 2.5 km away from the closest rupture plane), the overall low percentage may reflect our limited knowledge of the stress and slip variability along the fault plane, nonplanar fault geometry, and stress heterogeneities due to the mechanical properties of the faulted medium.

Our findings suggest that the volume of fluid injection may not limit the mainshock magnitude and/or cumulative moment release, as McGarr [2014] previously suggested. Static Coulomb stress changes due to Event A are consistent with triggering of Event B, which suggests that fluid induced events such as the $M5.0$ foreshock in Oklahoma, can trigger larger events if a nearby fault is critically stressed. This key, but not unexpected, observation has implications for estimating seismic hazard from injection.

Appendix A: Instrument Type and Data Logger Information

Table A1 contains general information regarding the seismic array deployed in the epicentral region of Events A–C. The main operating agencies are the University of Oklahoma Rapid Aftershock Mobilization Program (OU RAMP), the United States Geological Survey Pasadena, California, and Golden, Colorado offices, and the Array Network Facility, which manages the EarthScope Transportable Array. Information regarding the station names, instrument and data logger types, and sample rates (in Hz) are shown. The OU RAMP “LC” (Lincoln County, Oklahoma) stations are labeled by number only in Figure 1a, while the EarthScope TA stations are labeled in Figure 1b. Note that the sampling rate of stations LC01–LC03 was increased from 100 Hz to 250 Hz after the mainshock occurred.

Table A1. Instrument Type and Data Logger Information

Operating Agency	Station Names	Instrument Type	Data Logger Type	Sample Rate (in Hz)	Notes
OU RAMP	LC01–LC03	Nanometrics Trillium Compact	Taurus Standard 47 k	100	Sample rate changed after Event B
OU RAMP	LC01–LC03	Nanometrics Trillium Compact	Taurus Standard 47 k	250	
OU RAMP	LC04–LC08	Nanometrics Trillium Compact	Taurus Standard 47 k	250	
OU RAMP	LC09–LC10	Episensor	Reftek 130	250	
OU RAMP	LC11–LC18	Guralp CMG40T	Reftek 130	250	
USGS NetQuakes	OK001[2,4,5,8,9-12]	GeoSig Force Balance Accelerometer AC-63	GMS-18-NetQuakes	200	
USGS Golden	OK020–OK022	Nanometrics Trillium Compact	Reftek 130	40	
USGS Pasadena	OKR01–OKR10	Nanometrics Trillium Compact	Reftek 130	200	
EarthScope TA	TUL1, V35A, W35A, U35A, X36A	Streckeisen STS-2	Quanterra 330	40	
EarthScope TA	V36A	Guralp CMG3T	Quanterra 330	40	
EarthScope TA	W36A	Streckeisen STS-2.5	Quanterra 330	40	

Appendix B: Hypocentral Catalog

Table B1 is a compilation of the relative relocations of 110 earthquakes with A or B quality focal mechanism solutions. An identification number is for the 110 earthquakes relocated in this study, while a letter denotes the OGS locations of the three main events detailed in this study. Note that event #3 is the relative relocation of the *M*5.7 mainshock (Event B). The hypocenter date, time, and location are given, as well as the earthquake magnitude. For our relocations, the 2σ horizontal and vertical errors and the root-mean-square travel time residual from the *hypoDD* double-difference analysis are provided. Error information for Events A–C is provided by the OGS.

Table B1. Hypocenter Information and Constraints for 110 Earthquakes With A and B Quality Focal Mechanism Solutions

ID	Hypocenter Information						Hypocenter Constraints			
	Date (DD/MM/YYYY)	Time HH:MM:SS.SS	Location			<i>M</i>	Error (m)		RMS Travel Time Residual (s)	
			Latitude (°N)	Longitude (°E)	Depth (km)		Horizontal	Vertical		
A	05/11/2011	07:12:47.00	35.534	−96.766	3.40	5.0	1850	7400	0.8660	
1	05/11/2011	07:27:19.14	35.529	−96.768	6.13	3.3	87.20	751.40	0.1150	
2	05/11/2011	09:12:11.14	35.523	−96.776	4.24	3.3	68.30	434.20	0.0910	
3	06/11/2011	03:53:09.78	35.526	−96.780	4.27	5.6	88.20	182.70	0.1070	
B	06/11/2011	03:53:11.00	35.522	−96.780	3.10	5.7	1400	5700	0.7210	
4	06/11/2011	04:03:41.59	35.521	−96.782	5.29	4.0	65.70	104.60	0.0910	
5	06/11/2011	04:31:48.40	35.537	−96.761	10.54	3.9	84.30	167.60	0.1600	
6	06/11/2011	04:53:59.12	35.537	−96.759	6.13	3.3	66.00	101.50	0.1340	
7	06/11/2011	08:14:13.15	35.526	−96.779	5.65	3.1	61.50	86.80	0.1080	
8	06/11/2011	10:52:35.06	35.521	−96.784	3.83	3.6	59.85	91.00	0.1090	
9	07/11/2011	01:17:13.28	35.521	−96.784	6.03	3.0	52.35	62.20	0.0990	
10	07/11/2011	01:26:31.12	35.513	−96.793	3.80	3.4	54.25	69.30	0.1330	
11	07/11/2011	02:38:19.42	35.536	−96.760	8.64	3.1	58.60	68.70	0.1280	
12	07/11/2011	03:34:04.93	35.529	−96.766	5.47	2.5	60.30	77.00	0.0850	
13	07/11/2011	09:32:53.68	35.520	−96.806	4.88	3.0	69.55	86.80	0.1210	
14	07/11/2011	17:09:51.47	35.504	−96.799	4.69	3.2	67.00	86.90	0.1020	
C	08/11/2011	02:46:56.00	35.519	−96.792	2.50	5.0	2900	6900	1.5440	
15	08/11/2011	19:05:17.24	35.513	−96.828	6.11	3.5	56.00	86.20	0.2090	
16	09/11/2011	10:11:40.45	35.521	−96.800	4.44	3.0	47.70	54.80	0.0990	
17	09/11/2011	12:08:36.25	35.529	−96.766	4.00	3.4	43.55	59.80	0.0900	
18	10/11/2011	00:09:10.37	35.513	−96.804	7.66	1.1	51.75	71.00	0.0890	
19	10/11/2011	01:25:51.54	35.513	−96.792	3.70	1.2	35.60	57.60	0.1460	
20	10/11/2011	04:05:54.56	35.532	−96.770	5.88	0.6	52.20	74.40	0.0790	
21	10/11/2011	04:22:58.68	35.533	−96.761	5.62	1.4	36.30	59.60	0.0940	
22	10/11/2011	04:58:13.88	35.520	−96.789	5.82	0.7	41.40	65.70	0.0910	
23	10/11/2011	05:08:25.96	35.533	−96.761	5.74	1.1	45.35	69.60	0.1100	
24	10/11/2011	05:14:48.69	35.533	−96.761	5.80	1.4	33.10	54.30	0.1030	
25	10/11/2011	05:33:41.72	35.520	−96.806	4.59	1.1	45.65	66.00	0.1030	
26	10/11/2011	06:47:04.56	35.517	−96.785	3.80	1.3	34.65	55.70	0.1310	
27	10/11/2011	06:54:59.15	35.517	−96.787	3.77	0.8	30.55	49.20	0.0900	
28	10/11/2011	07:53:35.13	35.519	−96.785	5.62	0.7	39.10	65.00	0.0960	
29	10/11/2011	07:54:18.07	35.515	−96.789	3.83	2.1	28.95	45.80	0.1630	
30	10/11/2011	08:05:55.66	35.514	−96.792	3.40	0.8	35.35	61.80	0.0870	
31	10/11/2011	08:35:39.06	35.518	−96.789	7.25	0.6	37.70	64.30	0.0670	
32	10/11/2011	08:36:38.28	35.483	−96.850	3.71	3.2	34.45	52.20	0.1380	
33	10/11/2011	08:44:41.30	35.532	−96.771	6.66	1.7	41.15	64.90	0.0900	
34	10/11/2011	09:00:27.28	35.503	−96.804	4.09	1.6	50.80	92.40	0.0660	
35	10/11/2011	09:00:44.58	35.503	−96.804	3.84	2.8	45.00	96.40	0.0750	
36	10/11/2011	09:24:16.32	35.479	−96.854	3.40	0.8	41.60	70.20	0.1430	
37	10/11/2011	09:41:29.54	35.480	−96.852	1.46	1.8	50.75	50.60	0.1650	
38	10/11/2011	10:30:12.57	35.521	−96.786	4.83	1.4	38.65	55.30	0.0750	
39	10/11/2011	11:02:59.63	35.511	−96.801	7.53	0.9	38.50	60.10	0.1070	
40	10/11/2011	12:19:24.03	35.555	−96.751	4.69	1.0	40.55	47.00	0.1080	
41	10/11/2011	17:38:27.88	35.524	−96.771	3.89	1.6	42.95	59.80	0.0810	
42	10/11/2011	18:46:48.11	35.534	−96.770	9.33	1.3	48.40	65.40	0.1270	
43	10/11/2011	19:21:20.13	35.534	−96.757	5.21	1.7	36.75	54.90	0.1170	
44	10/11/2011	21:48:34.75	35.532	−96.763	5.20	2.0	43.35	65.10	0.0540	
45	10/11/2011	21:48:46.09	35.525	−96.771	3.86	2.2	41.20	72.60	0.0720	
46	10/11/2011	21:49:36.41	35.470	−96.758	3.20	1.8	42.70	85.20	0.8970	
47	10/11/2011	22:30:48.67	35.534	−96.765	7.30	2.2	42.20	61.50	0.1920	

Table B1. (continued)

ID	Hypocenter Information						Hypocenter Constraints			
	Date (DD/MM/YYYY)	Time HH:MM:SS.SS	Location			M	Error (m)		RMS Travel Time Residual (s)	
			Latitude (°N)	Longitude (°E)	Depth (km)		Horizontal	Vertical		
48	10/11/2011	22:46:23.01	35.521	-96.787	6.00	2.0	31.80	49.50	0.1320	
49	11/11/2011	01:00:37.33	35.517	-96.787	3.80	1.1	36.50	61.80	0.0820	
50	11/11/2011	02:26:38.45	35.530	-96.767	4.13	1.1	36.40	59.60	0.0800	
51	11/11/2011	03:05:04.59	35.491	-96.827	4.84	1.8	36.15	51.30	0.0990	
52	11/11/2011	03:16:07.72	35.523	-96.780	6.64	1.0	37.30	58.40	0.0730	
53	11/11/2011	10:29:00.86	35.524	-96.774	3.99	2.7	31.90	49.20	0.1030	
54	11/11/2011	19:19:15.49	35.534	-96.757	4.95	3.2	30.05	47.10	0.1340	
55	12/11/2011	01:18:42.42	35.544	-96.735	4.89	3.1	34.45	50.00	0.1470	
56	12/11/2011	01:41:02.69	35.534	-96.759	5.97	3.2	30.30	51.70	0.1160	
57	12/11/2011	03:56:54.19	35.529	-96.767	3.68	2.6	29.50	49.00	0.1010	
58	12/11/2011	08:55:40.82	35.493	-96.829	4.70	2.5	37.45	61.00	0.0890	
59	14/11/2011	01:38:32.91	35.514	-96.796	6.82	2.8	31.60	51.90	0.1300	
60	14/11/2011	05:31:41.66	35.514	-96.793	3.81	3.2	28.05	32.90	0.1360	
61	14/11/2011	05:37:26.33	35.518	-96.783	3.58	2.3	31.00	49.30	0.1370	
62	14/11/2011	06:14:03.36	35.516	-96.787	3.79	1.2	27.40	48.30	0.1180	
63	14/11/2011	07:14:54.10	35.533	-96.758	5.97	1.6	29.35	50.80	0.1150	
64	14/11/2011	08:27:29.21	35.533	-96.768	6.06	1.9	37.45	63.80	0.1400	
65	14/11/2011	12:16:20.61	35.534	-96.759	5.68	2.2	28.55	52.30	0.1080	
66	14/11/2011	12:18:41.97	35.540	-96.770	8.92	1.5	43.15	57.80	0.2860	
67	14/11/2011	13:45:36.43	35.538	-96.752	4.91	1.6	31.45	48.70	0.1080	
68	14/11/2011	16:11:43.29	35.534	-96.759	5.71	1.6	24.40	45.20	0.1440	
69	14/11/2011	20:26:39.35	35.542	-96.758	4.33	2.5	31.80	49.70	0.1300	
70	14/11/2011	23:48:36.31	35.472	-96.872	4.05	2.4	30.00	47.40	0.2160	
71	15/11/2011	00:48:37.96	35.533	-96.759	5.99	1.9	26.90	49.10	0.0940	
72	15/11/2011	00:57:12.14	35.526	-96.776	5.35	2.2	36.85	57.20	0.0740	
73	15/11/2011	06:20:40.51	35.519	-96.789	7.21	2.0	29.35	45.30	0.1110	
74	15/11/2011	06:35:22.18	35.512	-96.806	7.23	1.5	35.90	54.70	0.1120	
75	15/11/2011	09:46:30.48	35.538	-96.757	5.61	1.9	29.55	53.40	0.1170	
76	15/11/2011	14:22:38.92	35.534	-96.759	5.75	0.7	26.10	44.90	0.1210	
77	15/11/2011	16:04:40.70	35.558	-96.748	2.86	1.6	33.85	52.30	0.1230	
78	16/11/2011	00:32:28.22	35.505	-96.810	4.57	0.9	28.10	46.60	0.1320	
79	16/11/2011	00:39:09.53	35.519	-96.787	5.46	1.5	29.50	51.60	0.0850	
80	16/11/2011	03:52:39.17	35.465	-96.749	3.45	1.4	40.35	114.10	0.7210	
81	16/11/2011	05:17:10.74	35.521	-96.788	5.46	2.8	32.15	53.20	0.1080	
82	16/11/2011	06:16:42.95	35.464	-96.742	3.81	1.3	37.70	105.80	0.5380	
83	16/11/2011	07:21:23.28	35.550	-96.755	4.23	1.0	28.00	46.70	0.1500	
84	16/11/2011	08:34:31.27	35.512	-96.806	7.72	1.6	34.20	54.30	0.1020	
85	16/11/2011	12:14:08.60	35.532	-96.764	9.50	2.3	36.85	52.70	0.1170	
86	16/11/2011	15:27:15.76	35.520	-96.783	5.56	2.7	26.90	47.10	0.1100	
87	16/11/2011	17:10:51.56	35.498	-96.804	4.38	3.2	31.65	49.40	0.1470	
88	17/11/2011	02:06:23.35	35.499	-96.819	5.20	1.5	36.80	54.50	0.1210	
89	17/11/2011	09:03:10.68	35.523	-96.775	4.33	1.6	31.25	46.40	0.1360	
90	17/11/2011	10:57:33.50	35.535	-96.762	6.02	1.5	26.95	49.40	0.1160	
91	17/11/2011	12:00:56.75	35.535	-96.757	5.25	1.6	30.35	50.90	0.1070	
92	17/11/2011	12:06:42.78	35.537	-96.754	6.24	1.7	36.35	57.80	0.1590	
93	17/11/2011	20:51:16.51	35.543	-96.753	3.52	2.3	26.40	49.40	0.1330	
94	17/11/2011	21:22:21.10	35.520	-96.788	8.30	2.0	34.45	56.00	0.1000	
95	18/11/2011	04:45:45.97	35.519	-96.788	6.48	2.3	27.05	45.30	0.1400	
96	18/11/2011	05:50:39.58	35.535	-96.769	8.33	2.3	32.00	50.00	0.1570	
97	18/11/2011	07:41:07.61	35.537	-96.762	9.09	3.3	35.90	50.10	0.1530	
98	20/11/2011	05:54:01.85	35.550	-96.752	4.36	2.8	25.40	40.40	0.1310	
99	21/11/2011	10:45:37.75	35.549	-96.750	3.72	2.5	28.65	46.90	0.1290	
100	21/11/2011	21:46:08.97	35.504	-96.813	5.57	3.0	35.45	59.80	0.1110	
101	22/11/2011	07:39:58.19	35.525	-96.778	8.75	2.5	33.80	51.60	0.0830	
102	24/11/2011	21:11:03.69	35.536	-96.770	8.67	3.7	31.10	48.50	0.1690	
103	25/11/2011	21:24:29.04	35.508	-96.749	6.05	3.4	43.40	64.00	0.1010	
104	29/11/2011	09:22:32.66	35.534	-96.765	5.85	2.7	36.30	63.40	0.0950	
105	01/12/2011	10:18:16.30	35.547	-96.757	3.87	2.6	32.05	63.30	0.1380	
106	03/12/2011	04:42:11.66	35.529	-96.769	9.42	3.3	37.50	56.20	0.1570	
107	03/12/2011	15:45:00.86	35.535	-96.758	5.28	2.5	31.65	51.00	0.1150	
108	06/12/2011	19:00:52.14	35.531	-96.765	5.67	2.8	38.75	72.90	0.0810	
109	16/12/2011	18:17:18.62	35.531	-96.765	4.44	2.6	31.65	44.30	0.1290	
110	22/12/2011	04:14:33.66	35.494	-96.832	5.61	2.6	33.35	58.20	0.1260	

Appendix C: Focal Mechanism Catalog

Table C1 is a compilation of the 110 A and B quality focal mechanism solutions. The number in the first column is the event number for each earthquake, while the letter denotes the GCMT solution of Events A–C. The magnitude of the event (*M*) is also given and is the same as Table B1. The focal mechanism parameters of the best fit double-couple solutions are presented in Table C1, including the plunge (δ) and azimuth (ϵ) of the compressional (*P*), null (*B*), and tensional (*T*) axes, as well as the strike (ϕ), dip (θ), and rake (λ) of the two nodal planes. In addition, the number of *P* wave and *S* wave picks and *S/P* amplitude ratio observations (NOBS), the focal plane uncertainty (FPU), azimuthal station gap (GAP), and the quality of the HASH focal mechanism solution [Hardebeck and Shearer, 2002, 2003] are also provided.

Table C1. Principal Axes, Double-Couple Component Focal Mechanisms, and Constraints

ID	<i>M</i>	Principal Axes						Focal Mechanism Solution						Focal Mechanism Constraints			
		<i>P</i> axis		<i>B</i> axis		<i>T</i> axis		Nodal Plane 1			Nodal Plane 2			NOBS	FPU (deg)	GAP (deg)	Quality
		δ	ϵ	δ	ϵ	δ	ϵ	ϕ	θ	λ	ϕ	θ	λ				
A	5.0	16	164	72	315	8	72	207	73	175	299	85	17	GCMT solution			
1	3.3	1	85	71	353	19	176	219	76	167	312	77	14	17	27	81	B
2	3.3	0	274	67	5	23	184	227	74	163	322	74	17	20	23	82	A
3	5.6	1	98	77	4	13	188	232	80	171	323	81	10	16	34	83	B
B	5.7	0	189	87	91	3	279	54	88	−178	324	88	−2	GCMT solution			
4	4	10	97	63	347	25	192	232	65	169	327	80	25	24	26	83	B
5	3.9	4	89	56	354	34	182	220	64	157	320	69	28	22	33.5	78	B
6	3.3	6	95	67	351	22	187	229	70	168	323	79	20	22	22.5	63	A
7	3.1	3	89	51	356	39	182	218	61	152	322	66	32	27	17.5	82	A
8	3.6	6	92	61	352	28	185	225	66	163	322	75	25	22	21.5	84	A
9	3	6	298	75	53	13	207	252	85	166	343	76	5	31	12	84	A
10	3.4	1	90	61	358	29	180	221	69	159	319	70	22	25	18.5	86	A
11	3.1	29	88	60	286	8	182	229	64	−164	132	76	−27	25	20.5	58	A
12	2.5	71	359	11	124	15	217	118	61	−103	323	31	−68	24	17	63	A
13	3	13	233	75	88	8	325	279	87	−15	10	75	−177	27	31.5	80	B
14	3.2	16	233	74	58	1	323	277	80	−12	9	78	−170	27	22.5	88	A
C	5.0	15	314	73	160	7	46	91	74	6	359	84	164	GCMT solution			
15	3.5	20	89	51	331	32	192	227	52	171	322	83	38	35	15.5	85	A
16	3	12	222	77	19	5	131	266	78	−5	357	85	−168	35	13.5	68	A
17	3.4	4	66	86	228	1	336	201	88	−176	111	86	−2	34	19	44	A
18	1.1	32	45	5	312	58	214	311	77	85	154	14	112	31	21.5	61	A
19	1.2	6	287	49	24	41	193	233	67	145	338	58	27	29	17.5	60	A
20	0.6	9	80	77	214	9	348	214	90	−167	124	77	0	27	12	51	A
21	1.4	6	101	81	332	7	191	236	81	179	326	89	9	35	22.5	44	A
22	0.7	2	89	74	353	15	179	223	78	170	315	80	12	29	9.5	61	A
23	1.1	9	277	63	25	25	182	227	79	155	322	65	12	31	6	44	A
24	1.4	10	280	67	35	20	186	232	83	158	325	68	8	38	8	43	A
25	1.1	22	235	68	40	5	143	277	71	−12	11	79	−161	27	19	67	A
26	1.3	6	97	61	357	28	190	230	66	163	327	75	25	33	14	68	A
27	0.8	8	94	66	346	23	188	229	68	169	323	80	22	29	7.5	76	A
28	0.7	20	64	0	334	70	243	155	25	91	334	65	90	26	33	68	B
29	2.1	5	279	69	23	20	187	231	80	162	324	72	11	37	19.5	59	A
30	0.8	17	296	53	51	31	195	243	81	144	339	55	11	29	11	60	A
31	0.6	6	239	81	8	7	149	194	89	171	284	81	1	29	10	62	A
32	3.2	7	95	65	349	24	188	229	68	168	323	79	22	39	26	67	B
33	1.7	3	231	80	121	9	322	97	86	9	6	81	176	33	22	51	A
34	1.6	5	227	80	110	9	318	93	87	10	3	80	177	28	19	57	A
35	2.8	20	231	70	46	2	140	274	75	−13	8	77	−165	28	26.5	58	B
36	0.8	32	92	52	309	19	194	237	53	−169	140	81	−38	26	25.5	88	B
37	1.8	9	84	75	211	12	352	38	88	165	128	75	2	26	33	71	B
38	1.4	0	79	77	348	13	169	213	81	171	304	81	9	33	15.5	51	A
39	0.9	6	282	67	26	22	190	234	79	160	328	70	12	27	12	60	A
40	1	39	74	36	200	31	315	197	85	−126	100	36	−8	32	17	89	A
41	1.6	19	67	66	207	14	332	200	87	−156	109	66	−3	39	15.5	46	A
42	1.3	23	99	64	250	11	4	233	82	−155	139	65	−9	31	6	54	A
43	1.7	11	252	77	109	8	343	28	77	−178	297	88	−13	33	23.5	48	A
44	2	2	98	70	4	20	189	232	75	167	325	77	15	32	11	62	A
45	2.2	7	57	3	326	82	212	150	38	95	324	52	86	28	34	64	B
46	1.8	22	87	67	280	5	179	225	71	−167	131	78	−19	45	24.5	69	A
47	2.2	10	285	18	192	69	44	36	38	120	180	58	69	41	24	48	A

Table C1. (continued)

ID	M	Principal Axes						Focal Mechanism Solution						Focal Mechanism Constraints			
		P axis		B axis		T axis		Nodal Plane 1			Nodal Plane 2			NOBS	FPU (deg)	GAP (deg)	Quality
		δ	ϵ	δ	ϵ	δ	ϵ	ϕ	θ	λ	ϕ	θ	λ				
48	2	15	31	41	288	45	137	271	71	46	163	47	154	39	14	78	A
49	1.1	13	291	37	31	49	185	229	68	131	342	46	32	29	21	66	A
50	1.1	10	262	74	29	13	170	216	88	164	306	74	2	38	14	40	A
51	1.8	12	95	77	298	5	186	231	78	-175	140	85	-12	41	19	63	A
52	1	49	124	41	299	3	31	269	60	-139	155	55	-37	33	20.5	66	A
53	2.7	1	96	71	4	19	187	230	76	167	323	77	14	62	14.5	51	A
54	3.2	3	254	74	153	15	344	28	77	171	120	81	13	70	11	29	A
55	3.1	0	282	67	13	23	192	235	74	163	330	74	17	70	16.5	39	A
56	3.2	12	277	66	35	20	183	229	84	157	321	67	7	66	9.5	29	A
57	2.6	3	59	80	165	10	328	104	81	5	13	85	171	57	22	36	A
58	2.5	20	103	47	349	36	208	240	49	167	339	80	42	59	18	62	A
59	2.8	6	285	71	34	18	193	238	82	163	330	73	8	57	10.5	62	A
60	3.2	5	93	64	353	25	185	226	69	165	321	76	22	71	18.5	60	A
61	2.3	11	271	70	33	17	178	224	86	160	315	70	4	39	23.5	84	A
62	1.2	20	295	66	77	14	200	68	86	-156	336	66	-4	46	12	59	A
63	1.6	15	272	65	38	20	177	224	87	155	315	65	3	52	10	47	A
64	1.9	16	87	73	246	5	355	222	83	-165	130	75	-7	63	10	30	A
65	2.2	16	285	58	43	27	187	234	83	149	328	59	8	51	9	40	A
66	1.5	8	278	27	184	62	22	35	44	130	166	58	58	34	31.5	40	B
67	1.6	11	294	78	100	3	203	69	84	-170	338	80	-6	42	12.5	47	A
68	1.6	7	277	70	27	18	185	230	82	162	322	72	8	46	9.5	42	A
69	2.5	15	280	71	138	11	13	57	71	-177	326	87	-19	65	10	37	A
70	2.4	17	92	71	297	8	184	229	72	-173	137	83	-18	44	27.5	79	B
71	1.9	8	102	76	336	11	194	238	76	178	328	88	14	45	9	39	A
72	2.2	31	303	55	93	14	205	77	79	-147	340	58	-13	57	10.5	54	A
73	2	47	120	4	26	43	292	206	88	-86	321	4	-155	46	11.5	61	A
74	1.5	31	75	35	321	40	196	220	35	171	317	85	55	52	15.5	60	A
75	1.9	36	45	52	243	9	142	88	72	-34	190	58	-159	58	15.5	30	A
76	0.7	16	270	57	26	28	172	219	82	148	314	58	9	41	13.5	50	A
77	1.6	14	253	59	7	27	156	202	81	150	297	60	10	26	18	46	A
78	0.9	26	79	53	209	24	336	208	89	-143	117	53	-1	38	7	57	A
79	1.5	3	70	61	335	29	162	202	68	161	299	72	23	44	10.5	59	A
80	1.4	31	85	59	262	2	354	224	70	-156	125	68	-22	45	32.5	78	B
81	2.8	9	40	77	174	9	308	84	77	0	354	90	167	66	11.5	62	A
82	1.3	6	88	76	330	12	179	223	77	176	314	86	13	44	26	86	B
83	1	11	246	79	47	3	155	21	85	-170	290	80	-5	47	14	41	A
84	1.6	27	68	17	329	57	209	193	24	137	323	74	72	44	12	60	A
85	2.3	4	294	85	148	3	24	69	85	-179	339	89	-5	59	6.5	27	A
86	2.7	19	96	71	270	2	5	232	78	-165	139	75	-12	68	13	34	A
87	3.2	13	233	76	77	6	324	278	85	-13	9	77	-175	72	20.5	51	A
88	1.5	1	243	81	149	9	333	109	84	7	18	83	174	46	18	63	A
89	1.6	13	93	71	320	13	187	230	71	180	320	90	19	51	10.5	53	A
90	1.5	23	83	62	298	14	179	223	63	-173	130	84	-27	50	11.5	29	A
91	1.6	14	262	76	83	0	352	38	80	-170	306	80	-10	55	12	29	A
92	1.7	21	263	65	115	12	358	42	66	-173	309	84	-24	54	8.5	29	A
93	2.3	14	270	68	142	17	5	47	68	178	138	88	22	52	13	42	A
94	2	7	96	69	349	20	189	231	71	170	324	81	19	48	13.5	61	A
95	2.3	28	351	42	233	36	103	229	85	48	134	42	173	55	9	60	A
96	2.3	0	92	69	1	21	182	225	75	165	319	76	16	63	9	29	A
97	3.3	11	97	79	278	0	187	233	82	-172	142	82	-8	71	11	29	A
98	2.8	3	246	87	39	1	156	291	87	-1	21	89	-177	70	19	38	A
99	2.5	2	256	88	58	1	166	31	89	-178	301	88	-1	63	15	40	A
100	3	2	99	74	1	16	189	233	77	170	325	80	13	74	14	52	A
101	2.5	15	171	55	58	31	271	44	80	34	307	57	168	57	10.5	57	A
102	3.7	11	91	78	297	5	182	227	79	-176	136	86	-11	78	10.5	27	A
103	3.4	22	271	63	56	14	175	44	84	-154	311	64	-7	77	11	35	A
104	2.7	25	85	64	280	6	178	224	68	-166	129	77	-23	61	13	47	A
105	2.6	8	74	80	215	6	343	209	89	-170	119	80	-1	44	16.5	69	A
106	3.3	16	281	73	119	5	13	58	75	-172	326	82	-15	65	7	40	A
107	2.5	14	259	74	52	7	167	34	85	-165	303	75	-5	61	9.5	53	A
108	2.8	29	94	54	313	19	195	237	55	-172	142	83	-35	61	12	40	A
109	2.6	18	260	71	71	3	169	36	79	-165	303	75	-11	54	18.5	40	A
110	2.6	12	102	77	299	4	193	238	79	-174	147	84	-11	64	14	60	A

Acknowledgments

The U.S. Geological Survey, Oklahoma Geological Survey, Oklahoma State University, and the University of Oklahoma provided personnel to assist with field installations. The University of Oklahoma and U.S. Geological Survey funded field acquisition costs. The PASSCAL instrument center and U.S. Geological Survey provided RAMP instruments and logistical support. We gratefully acknowledge the discussions with H. Meighan and the reviews provided by J. Hardebeck, T. Parsons, D. Kilb, and an anonymous reviewer. Funding provided by NSF EAR-PF-1049609 (D.F. Sumy), and the IRIS Summer Internship Program (M. Wei) supported this research.

References

- Beeler, N. M., R. W. Simpson, S. H. Hickman, and D. A. Lockner (2000), Pore fluid pressure, apparent friction, and Coulomb failure, *J. Geophys. Res.*, *105*, 25,533–25,542.
- Cocco, M., and J. R. Rice (2002), Pore pressure and poroelasticity effects in Coulomb stress analysis of earthquake interactions, *J. Geophys. Res.*, *107*(B2), 2030, doi:10.1029/2000JB000138.
- Cochran, E. S., J. E. Vidale, and S. Tanaka (2004), Earth tides can trigger shallow thrust fault earthquakes, *Science*, *306*, 1164–1166.
- Crone, T. J., M. Tolstoy, and D. F. Stroup (2011), Permeability structure of young ocean crust from poroelastically triggered microearthquakes, *Geophys. Res. Lett.*, *38*, L05305, doi:10.1029/2011GL046820.
- Daniel, G., et al. (2011), Changes in effective stress during the 2003–2004 Ubaye seismic swarm, France, *J. Geophys. Res.*, *116*, B01309, doi:10.1029/2010JB007551.
- Dodge, D. A., G. C. Beroza, and W. L. Ellsworth (1995), Foreshock sequence of the 1992 Landers, California, earthquake and its implications for earthquake nucleation, *J. Geophys. Res.*, *100*(B7), 9685–9880.
- Dodge, D. A., G. C. Beroza, and W. L. Ellsworth (1996), Detailed observations of California foreshock sequences: Implications for the earthquake initiation process, *J. Geophys. Res.*, *101*(B10), 22,371–22,392.
- Durand, V., M. Bouchon, H. Karabulut, D. Marsan, J. Schmittbuhl, M. P. Bouin, M. Aktar, and G. Daniel (2010), Seismic interaction and delayed triggering along the North Anatolian Fault, *Geophys. Res. Lett.*, *37*, L18310, doi:10.1029/2010GL044688.
- Engiel, J. F., D. A. Wiens, and S. Stein (1986), Mechanisms and depths of Atlantic transform earthquakes, *J. Geophys. Res.*, *91*, 548–577.
- Felzer, K. R., and E. E. Brodsky (2005), Testing the stress shadow hypothesis, *J. Geophys. Res.*, *110*, B05S09, doi:10.1029/2004JB003277.
- Gahalaut, K., and A. Hassoup (2012), Role of fluids in the earthquake occurrence around Aswan reservoir, Egypt, *J. Geophys. Res.*, *117*, B02303, doi:10.1029/2011JB008796.
- Gomberg, J., P. A. Reasenber, P. Bodin, and R. A. Harris (2001), Earthquake triggering by seismic waves following the Landers and Hector Mine earthquakes, *Nature*, doi:10.1038/35078053.
- Gomberg, J., P. Bodin, and P. A. Reasenber (2003), Observing Earthquakes Triggered in the Near Field by Dynamic Deformations, *Bull. Seismol. Soc. Am.*, *93*, 118–138.
- Green, D. H., and H. F. Wang (1986), Fluid pressure response to undrained compression in saturated sedimentary rock, *Geophysics*, *51*, 948–956.
- Guglielmi, Y., F. Cappa, and D. Amitrano (2008), High-definition analysis of fluid-induced seismicity related to the mesoscale hydromechanical properties of a fault zone, *Geophys. Res. Lett.*, *35*, L06306, doi:10.1029/2007GL033087.
- Hainzl, S., and D. Marsan (2008), Dependence of the Omori-Utsu law parameters on mainshock magnitude: Observations and modeling, *J. Geophys. Res.*, *113*, B10309, doi:10.1029/2008JB006011.
- Hainzl, S., and Y. Ogata (2005), Detecting fluid signals in seismicity data through statistical earthquake modeling, *J. Geophys. Res.*, *110*, B05S07, doi:10.1029/2004JB003247.
- Hainzl, S., B. Enescu, M. Cocco, J. Woessner, C. Catalli, R. Wang, and F. Roth (2009), Aftershock modeling based on the uncertain stress calculations, *J. Geophys. Res.*, *114*, B05S07, doi:10.1029/2004JB003247.
- Hainzl, S., S. Steacy, and D. Marsan (2010), Seismicity models based on Coulomb stress calculations, Community Online Resource for Statistical Seismicity Analysis, doi:10.5078/corssa-32035809. [Available at <http://www.corssa.org>.]
- Hardebeck, J. L., and P. M. Shearer (2002), A new method for determining first-motion focal mechanisms, *Bull. Seismol. Soc. Am.*, *92*, 2264–2276, doi:10.1785/0120010200.
- Hardebeck, J. L., and P. M. Shearer (2003), Using S/P amplitude ratios to constrain the focal mechanisms of small earthquakes, *Bull. Seismol. Soc. Am.*, *93*, 2434–2444, doi:10.1785/0120020236.
- Hardebeck, J. L., and A. J. Michael (2006), Damped regional-scale stress inversions: Methodology and examples for southern California and the Coalinga aftershock sequence, *J. Geophys. Res.*, *111*, B11310, doi:10.1029/2005JB004144.
- Hardebeck, J. L., J. J. Nazareth, and E. Hauksson (1998), The static stress change triggering model: Constraints from two southern California aftershock sequences, *J. Geophys. Res.*, *103*(B10), 24,427–24,437.
- Harris, R. A. (1998), Introduction to special section: Stress triggers, stress shadows, and implications for seismic hazard, *J. Geophys. Res.*, *103*, 24,347–24,358.
- Hart, D. J. (1994), Laboratory measurements of a complete set of poroelastic moduli for Berea sandstone and Indiana limestone, M. S. thesis, Univ. of Wisconsin, Madison, Wis.
- Helmstetter, A., and B. E. Shaw (2006), Relation between stress heterogeneity and aftershock rate in the rate-and-state model, *J. Geophys. Res.*, *111*, B07304, doi:10.1029/2005JB004077.
- Horton, S. (2012), Disposal of Hydrofracking Waste Fluid by Injection into Subsurface Aquifers Triggers Earthquake Swarm in Central Arkansas with Potential for Damaging Earthquake, *Seismol. Res. Lett.*, *83*(2), doi:10.1785/gssrl.83.2.250.
- Joseph, L. (1987), Subsurface analysis, “Cherokee” Group (Des Moinesian), portions of Lincoln, Pottawatomie, Seminole, and Okfuskee Counties, Oklahoma: The Shale Shaker, v.12, p. 44–69.
- Keranen, K. M., H. M. Savage, G. A. Abers, and E. S. Cochran (2013), Potentially induced earthquakes in Oklahoma, USA: Links between wastewater injection and the 2011 M_w 5.7 earthquake sequence, *Geology*, doi:10.1130/G34045.1.
- Kilb, D., and J. L. Hardebeck (2006), Fault Parameter Constraints Using Relocated Earthquakes: A Validation of First Motion Focal Mechanism Data, *Bull. Seismol. Soc. Am.*, *96*, 1140–1158.
- Kilb, D., M. Ellis, J. Gomberg, and S. Davis (1997), On the origin of diverse aftershock mechanisms following the 1989 Loma Prieta earthquake, *Geophys. J. Int.*, *128*, 557–570.
- Kim, W.-Y. (2013), Induced seismicity associated with fluid injection into a deep well in Youngstown, Ohio, *J. Geophys. Res. Solid Earth*, *118*, 3506–3518, doi:10.1002/jgrb.50247.
- King, G. C. P., and M. Cocco (2001), Fault interaction by elastic stress changes: New clues from earthquake sequences, *Adv. Geophys.*, *44*, 1–38.
- King, G. C. P., R. S. Stein, and J. Lin (1994), Static Stress Changes and the Triggering of Earthquakes, *Bull. Seismol. Soc. Am.*, *84*, 935–953.
- Kissling, E. (1988), Geotomography with local earthquake data, *Rev. Geophys.*, *26*, 659–698.
- Kissling, E., W. L. Ellsworth, D. Eberhart-Phillips, and U. Kradolfer (1994), Initial reference models in local earthquake tomography, *J. Geophys. Res.*, *99*, 19,635–19,646.
- Klein, F. W. (2002), User’s Guide to HYPOINVERSE 2000, a Fortran Program to Solve for Earthquake Locations and Magnitudes, *U.S. Geol. Surv. Open-File Rept. 02-171*, 113 pp.
- Kroll, K., E. S. Cochran, K. Richards-Dinger, and D. F. Sumy (2013), Aftershocks of the 2010 M_w 7.2 El Mayor-Cucapah earthquake reveal complex faulting in the Yuha Desert, California, *J. Geophys. Res. Solid Earth*, 6146–6164, doi:10.1002/2013JB010529.

- Liu, P., and R. J. Archuleta (2004), A new nonlinear finite fault inversion with three-dimensional Green's functions: Application to the 1989 Loma Prieta, California, earthquake, *J. Geophys. Res.*, *109*, B02318, doi:10.1029/2003JB002625.
- Llenos, A., and A. Michael (2013), Modeling Earthquake Rate Changes in Oklahoma and Arkansas: Possible Signatures of Induced Seismicity, *Bull. Seismol. Soc. Am.*, *103*, 5, doi:10.1785/0120130017.
- Marsan, D. (2006), Can coseismic stress variability suppress seismicity shadows? Insights from a rate-and-state friction model, *J. Geophys. Res.*, *111*, B06305, doi:10.1029/2001JB000588.
- McGarr, A. (2014), Maximum magnitude earthquakes induced by fluid injection, *J. Geophys. Res. Solid Earth*, *119*, doi:10.1002/2013JB010597.
- Meltzer, A., et al. (1999), The USArray Initiative, *GSA Today*, *9*(11), 8–10.
- Michael, A. J. (1984), Determination of stress from slip data: Faults and folds, *J. Geophys. Res.*, *89*, 11,517–11,526.
- Michael, A. J. (1987), Use of focal mechanisms to determine stress: A control study, *J. Geophys. Res.*, *92*, 357–368.
- Nur, A., and J. R. Booker (1972), Aftershocks caused by pore fluid flow?, *Science*, *175*, 885–887.
- Okada, Y. (1992), Internal deformation due to shear and tensile faults in a half-space, *Bull. Seismol. Soc. Am.*, *82*(2), 1018–1040.
- Parsons, T. (2002), Global Omori law decay of triggered earthquakes: Large aftershocks outside the classical aftershock zone, *J. Geophys. Res.*, *107*(B9), 2199, doi:10.1029/2001JB000646.
- Parsons, T. (2008), Persistent earthquake clusters and gaps from slip on irregular faults, *Nat. Geosci.*, *1*, 59–63, doi:10.1038/ngeo.2007.36.
- Parsons, T., R. S. Stein, R. W. Simpson, and P. Reasenber (1999), Stress sensitivity of fault seismicity: A comparison between limited-offset oblique and major strike-slip faults, *J. Geophys. Res.*, *104*, 20,183–20,202.
- Parsons, T., Y. Ogata, J. Zhuang, and E. L. Geist (2012), Evaluation of static stress change forecasting with prospective and blind tests, *Geophys. J. Int.*, *188*, 1425–1440, doi:10.1111/j.1365-246X.2011.05343.x.
- Reasenber, P. A., and D. Oppenheimer (1985), FPFIT, FPLOT, and FPPAGE: Fortran computer programs for calculating and displaying earthquake fault-plane solutions, *U. S. Geol. Surv. Open-File Rep.* 85-739.
- Reasenber, P. A., and R. W. Simpson (1992), Response of regional seismicity to the static stress change produced by the Loma Prieta earthquake, *Science*, *255*, 1687–1690.
- Rice, J. R. (1992), Fault stress states, pore pressure distributions and the weakness of the San Andreas fault, in *Fault Mechanics and Transport Properties of Rock: A Festschrift in Honor of W. F. Brace*, edited by B. Evans and T.-F. Wong, pp. 475–503, Academic, San Diego, Calif.
- Rice, J. R., and M. P. Cleary (1976), Some basic stress diffusion solutions for fluid-saturated elastic porous media with compressible constituents, *Rev. Geophys.*, *14*, 227–241.
- Scherbaum, F., and M.-P. Bouin (1997), FIR filter effects and nucleation phases, *Geophys. J. Int.*, *130*, 661–668.
- Shapiro, S. A., J. Kummerow, C. Dinske, G. Asch, E. Rotherth, J. Erzinger, H.-J. Kumpel, and R. Kind (2006), Fluid induced seismicity guided by a continental fault: Injection experiment of 2004/2005 at the German Deep Drilling Site (KTB), *Geophys. Res. Lett.*, *33*, L01309, doi:10.1029/2005GL024659.
- Simpson, R. W., and P. A. Reasenber (1994), Earthquake-induced static stress changes on central California faults, in *The Loma Prieta, California Earthquake of October 17, 1989-Tectonic Processes and Models*, U.S. Geol. Surv. Prof. Pap., vol. 1550-F, edited by R. W. Simpson, pp. F55-F89, US Geological Survey, Washington, D. C.
- Smith, D. E., and J. H. Dieterich (2010), Aftershock Sequences Modeled with 3-D Stress Heterogeneity and Rate-State Seismicity Equations: Implications for Crustal Stress Estimation, *Pure Appl. Geophys.*, *167*, 1067–1085, doi:10.1007/s00024-010-0093-1.
- Steaey, S., D. Marsan, S. S. Nalbant, and J. McCloskey (2004), Sensitivity of static stress calculations to the earthquake slip distribution, *J. Geophys. Res.*, *109*, B04303, doi:10.1029/2002JB002365.
- Steaey, S., J. Gomberg, and M. Cocco (2005), Introduction to special section: Stress transfer, earthquake triggering, and time-dependent seismic hazard, *J. Geophys. Res.*, *110*, B05S01, doi:10.1029/2005JB003692.
- Stein, R. S. (1999), The role of stress transfer in earthquake occurrence, *Nature*, *402*(6762), 605–609.
- Stein, R. S., and M. Lisowski (1983), The 1979 Homestead Valley Earthquake Sequence, California: Control of Aftershocks and Postseismic Deformation, *J. Geophys. Res.*, *88*(B8), 6477–6490.
- Stein, R. S., G. C. P. King, and J. Lin (1992), Change in failure stress on the southern San Andreas fault system caused by the 1992 magnitude = 7.4 Landers earthquake, *Science*, *258*, 1328–1332.
- Stroup, D. F., D. R. Bohnenstiehl, M. Tolstoy, F. Waldhauser, and R. T. Weekly (2007), Pulse of the seafloor: Tidal triggering of microearthquakes at 9°50'N East Pacific Rise, *Geophys. Res. Lett.*, *34*, L15301, doi:10.1029/2007GL030088.
- Stroup, D. F., M. Tolstoy, T. J. Crone, A. Malinverno, and F. Waldhauser (2009), Systematic along-axis tidal triggering of microearthquakes observed at 9°50'N East Pacific Rise, *Geophys. Res. Lett.*, *36*, L18302, doi:10.1029/2009GL039493.
- Sumy, D. F., J. B. Gaherty, W.-Y. Kim, T. Diehl, and J. A. Collins (2013), The mechanisms of earthquakes and faulting in the southern Gulf of California, *Bull. Seismol. Soc. Am.*, *103*(1), doi:10.1785/0120120080.
- Toda, S., J. Lin, and R. S. Stein (2011a), Using the 2011 Mw 9.0 off the Pacific coast of Tohoku Earthquake to test the Coulomb stress triggering hypothesis and to calculate faults brought closer to failure, *Earth Planets Space*, *63*, 725–730.
- Toda, S., R. S. Stein, V. Sevilgen, and J. Lin (2011b), Coulomb 3.3 Graphic-Rich Deformation and Stress-Change Software for Earthquake, Tectonic, and Volcano Research and Teaching – User Guide, *U. S. Geol. Surv. Open-File Rep.* 2011-1060.
- Waldhauser, F. (2001), HypoDD – A program to compute double-difference hypocenter locations, *U.S. Geol. Survey, Open-File Rept.* 01-113, 25 pp.
- Waldhauser, F., and W. L. Ellsworth (2000), A double-difference earthquake location algorithm: Method and application to the Northern Hayward fault, California, *Bull. Seismol. Soc. Am.*, *90*, 1353–1368.
- Way, H. S. K. (1983), Structural study of the Hunton Lime of the Wilzetta Field, T12-13 N, R5E, Lincoln County, Oklahoma, pertaining to the exploration for hydrocarbons, M.S. thesis, Oklahoma State University, Stillwater, Oklahoma, U.S.A.
- Wells, D. L., and K. J. Coppersmith (1994), New empirical relationships among magnitude, rupture length, rupture width, rupture area, and surface displacement, *Bull. Seismol. Soc. Am.*, *84*(4), 974–1002.
- Yang, W., E. Hauksson, and P. M. Shearer (2012), Computing a Large Refined Catalog of Focal Mechanisms for Southern California (1981-2010): Temporal Stability of the Style of Faulting, *Bull. Seismol. Soc. Am.*, *102*, 1179–1194, doi:10.1785/0120110311.
- Zoback, M. D., and H.-P. Harjes (1997), Injection-induced earthquakes and crustal stress at 9 km depth at the KTB deep drilling site, Germany, *J. Geophys. Res.*, *102*(B8), 18,477–18,491.
- Zoback, M. D., and J. Townend (2001), Implications of hydrostatic pore pressures and high crustal strength for the deformation of intraplate lithosphere, *Tectonophysics*, *336*, 19–30.